JGR Atmospheres

RESEARCH ARTICLE
10.1029/2022JD036795

Wind, Rain, and the Closed to Open Cell Transition in Subtropical Marine Stratocumulus

Ryan Eastman[1], Isabel L. McCoy[2,3], and Robert Wood[1]

[1]University of Washington Department of Atmospheric Sciences, Seattle, WA, USA, [2]Rosenstiel School, University of Miami, Miami, FL, USA, [3]Cooperative Programs for the Advancement of Earth System Science, University Corporation for Atmospheric Research, Boulder, CO, USA

Key Points:

- A two-step process is associated with the closed-open cell transition: Strong winds precede intense rain; intense rain precedes the transition
- Strong wind is associated with intense rain and enhanced moisture flux and content in the closed cell Stratocumulus boundary layer
- Closed to disorganized transitions are preceded by a warm sea surface at long lead times and by dry air entrainment at short lead times

Supporting Information:

Supporting Information may be found in the online version of this article.

Correspondence to:

R. Eastman,
rmeast@atmos.washington.edu

Citation:

Eastman, R., McCoy, I. L., & Wood, R. (2022). Wind, rain, and the closed to open cell transition in subtropical marine stratocumulus. *Journal of Geophysical Research: Atmospheres*, *127*, e2022JD036795. https://doi.org/10.1029/2022JD036795

Received 18 MAR 2022
Accepted 20 SEP 2022

Abstract Lagrangian transitions in mesoscale cellular convective (MCC) clouds beginning as closed cell MCC and transitioning to open cells or disorganized but cellular MCC are explored on timescales from 12 to 72 hr. Potential drivers of MCC transitions are shown to act on multiple timescales. Closed-to-open MCC cloud transitions are preceded by strong surface winds and large moisture fluxes at lead times of up to 72 hr; and by high cloud water content, reduced cloud drop concentrations, and intense rain rates at lead times of 12–36 hr. The relationship between intense rain and the formation of open cells is consistent with a cold pool convergence mechanism. A Lagrangian analysis shows that anomalously strong surface winds are associated with higher rain rates as well as subsequent increases in rain rates through modifications to moisture flux and content in the boundary layer. The closed-open MCC transition contrasts with the closed-to-disorganized transition which at long lead times is associated with warm sea surface temperature and at diurnal-scale lead times is associated with variables related to cloud top entrainment drying such as a deepening boundary layer, weakening subsidence and inversion strength, and a drier free troposphere. A conceptual model is proposed where excess boundary layer moisture associated with wind breaks up stratocumulus through the closed-to-open transition, while excess dry-air entrainment at cloud top breaks up stratocumulus through the closed-to-disorganized transition.

1. Introduction

Over the eastern subtropical oceans, extensive warm and bright low-level stratocumulus (Sc) cloud decks cover the dark ocean surface, causing a cooling to the climate system by reflecting abundant sunlight and emitting infrared radiation (L'Ecuyer et al., 2019; Hartmann & Short, 1980). The spatial organization of this marine Sc assumes two dominant modes of mesoscale cellular convection (MCC): open and closed cells (Krueger & Fritz, 1961; Wood & Hartmann, 2006). Open cell MCC are characterized by narrow bands of heavily drizzling clouds in cell walls, situated between broad, open clear areas. Closed cells appear inverse to open, with broad, round regions of thick cloud bordered by more optically thin clouds or clear edges. Open cells are less-effective coolers of the climate compared to closed cells. In open cells, not only is cloud cover less extensive on average, but the clouds also tend to be optically thinner and less reflective (McCoy et al., 2017). These two modes of Sc organization coexist in similar climate regimes characterized by overlying subsidence, a cool sea surface, and a strong capping inversion (Norris, 1998; Wood, 2012). This coexistence drives interest in determining the processes controlling transitions from closed cells to open.

Further westward and offshore, Sc tends to evolve into disorganized cellular patterns as Sc is slowly replaced by cumulus clouds developing under the stratiform layer. Disorganized cloud patterns in the subtropical cloud regions tend to occur with lower cloud fractions, in reduced stability environments, and over warmer oceans (Bretherton et al., 2019). They also have a larger contribution from optically thin cloud features than in the near coastal cloud decks (O, Wood, Bretherton, et al., 2018; Wood et al., 2018). These features are thought to be generated through a deepening planetary boundary layer (PBL) and increased precipitation scavenging (O, Wood, Tseng, et al., 2018), leading to detrained layers with depleted cloud droplet number concentration aloft (Bretherton et al., 2019; O, Wood, Bretherton, 2018; O, Wood, Tseng, 2018).

Existing literature has established that cloud top cooling tends to drive circulations in closed cell MCC (Wood, 2012; Zhou & Bretherton, 2019), while precipitation may be essential in organizing and sustaining open cell MCC (Feingold et al., 2010; Yamaguchi & Feingold, 2015): Rain falling and evaporating into the subsaturated, sub-cloud boundary layer drives downdrafts due to evaporative cooling. Downdrafts create cold

pools (Terai & Wood, 2013) that diverge at the sea surface and then collide, forcing a convergence-driven rising motion between established raining elements, which has been seen to propagate an oscillating open cell regime in large-eddy scale simulations (Feingold et al., 2010).

An analysis of cloud morphologies in Mohrmann et al. (2021) shows that closed cell Sc tend to be observed in environments with surface wind divergence, while open cell Sc wind fields tend to be associated with surface wind convergence in the tropics and subtropics, but surface wind divergence in midlatitude marine cold air outbreaks. In McCoy et al. (2017), a global analysis, open cell MCC is observed to coincide with increased surface forcing associated with marine cold air outbreaks. Jensen et al. (2021) shows that open cell MCC occur in environments with stronger wind speed, greater vertical wind shear, stronger cold advection, and stronger rain rates in the North Atlantic Ocean, primarily for conditions of offshore flow originating from the North American continent. These analyses show that open and closed cell MCC tend to favor specific wind and flux environments within similar boundary layers, however the absence of a time dimension in those works means we cannot assess whether conditions associated with a certain morphology can also predict transitions between MCC types. Further, those studies represent differing study regions where differing large-scale climatological conditions may be associated with differing dominant cloud processes. This work is confined to warm boundary layer clouds in the subtropical oceans where climatological conditions are relatively homogeneous.

In Eastman et al. (2021), a Lagrangian analysis framework was developed to compare cloud scenes that evolved from closed to open MCC to those that remained closed cell MCC over a 24-hr period. That analysis, which was limited to the 24 hr surrounding the transition, showed that anomalously intense rainfall and stronger winds *precede* the closed-to-open transition by 12–24 hr. The more intense rain observed prior to the closed-to-open transition supports the hypothesis that cold pools associated with rainfall initiate the transition, but the role of wind speed was not clear, in part due to the restricted timescale of that analysis.

Prior studies have shown a tendency toward more intense rain in boundary layer clouds when wind speed is stronger (Lamer et al., 2020; Nuijens et al., 2009; Schulz et al., 2021), and also for deeper convective clouds (Back & Bretherton, 2005), but a mechanism has not been established. Additionally, Wood et al. (2008) and Jensen et al. (2021) show that open cell MCC conditions tend to coincide with windier environments, with Wood et al. (2008) going on to show that weak winds in the SE Pacific are likely associated with periods of reduced rainfall and declining cloud liquid water content. Finally, Scott et al. (2020) has shown, using deseasonalized and detrended monthly data, that stronger wind speeds are associated with increasing clouds in the subtropics, but with declines in cloud optical depth, further adding to evidence suggesting that wind speed may modify cloud properties.

In this study, we extend the 24-hour time range from Eastman et al. (2021) to 72 hr, adding two additional upstream days of data. This is done in order to further study the relationship between wind speed, precipitation, and the closed-open MCC transition. We will address several outstanding questions, motivated by our own prior work and the broader literature, including does wind speed affect the closed-open transition by mechanically rearranging or modifying clouds due to wind shear or divergence? Both Mohrmann et al. (2021) and Jensen et al. (2021) found differences in these fields between MCC classifications, and/or does wind speed modify surface fluxes as part of a process where an enhanced moisture source leads to enhanced rainfall; a more surface flux-based mechanism as suggested by McCoy et al. (2017). In this work, an additional 2 days of trajectory length combined with an expanded suite of predictor variables and a refined analysis compared to Eastman et al. (2021) will allow us to answer these questions and explore the relationships between cloud variables evolving together during this transition. Additionally, using this expanded time frame we are able to contrast the transition from closed-to-open MCC with the closed-to-disorganized MCC transition. We present our data and methods in Section 2, results in Section 3, validation tests, context, and data limitations discussions in Section 4, discussion in the context of existing literature in Section 5, and conclusions in Section 6.

2. Data and Lagrangian Framework

2.1. Lagrangian Trajectory Framework

Trajectories for this Lagrangian study are launched roughly 200 km apart along the CloudSat/CALIPSO track in four eastern subtropical ocean basins: the NE Pacific (15–30°N, 155–115°W), SE Pacific (5–30°S, 105–70°W), SE Atlantic (5–30°S, 15°W–15°E), and E Indian (20–30°S, 60–110°E). Originally, trajectories were launched

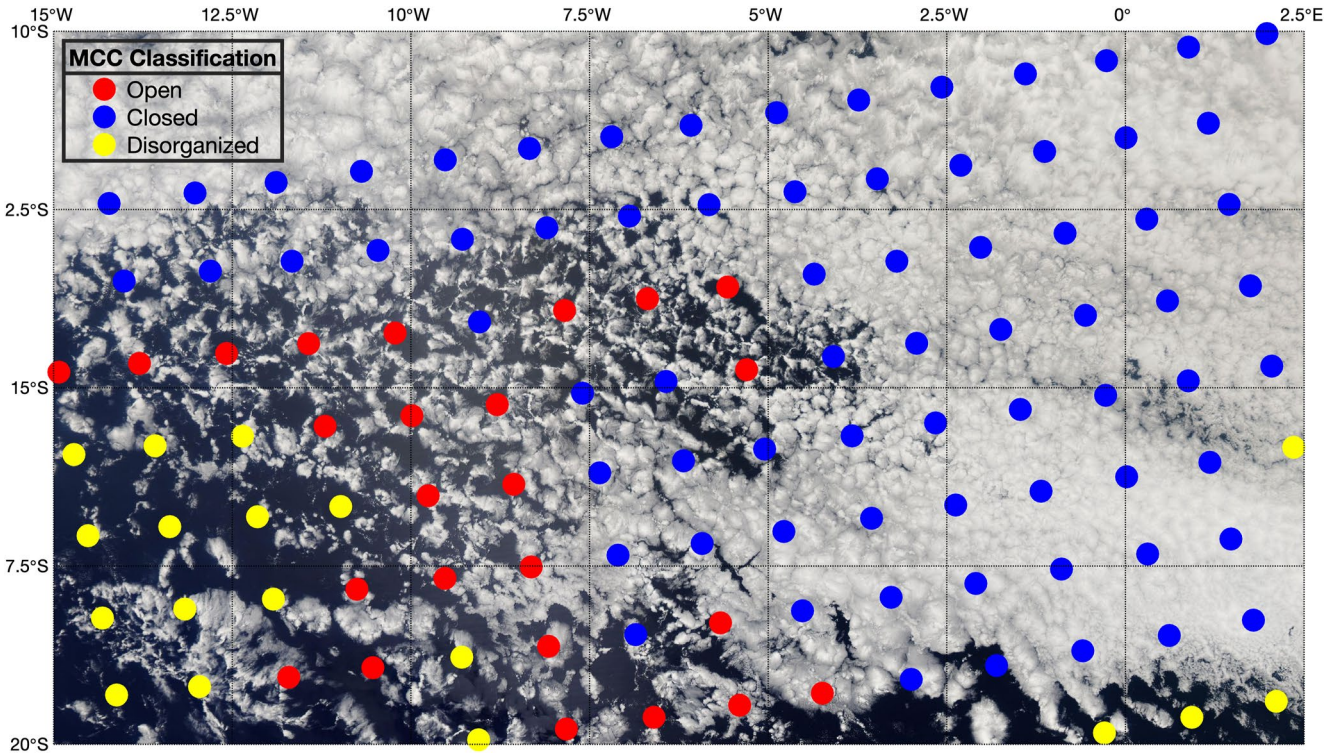

Figure 1. An example of the output of the mesoscale cellular convective classifier on a MODIS Aqua image taken on 25 September 2009 in the SE Atlantic region. Dots are spaced 128 km apart. Classified regions represent the 256 km^2 region surrounding each dot.

along the CloudSat/CALIPSO track to provide at least one data point that had CloudSat and CALIPSO data along with swath data from other polar orbiting satellites, which allowed for an independent check on several data products derived from wide data swaths. This expanded study does not directly rely on the CloudSat and CALIPSO instruments, though it uses data products derived from those sensors. Trajectories are produced for years 2007–2010 for all months, with ∼170,000 trajectories produced in total. Trajectories are run forward and backward from the launch point for 48 hr, and are driven by isobaric ERA-Interim (Dee et al., 2011) winds at 925 hPa. For data sets where day and night data are available, cloud scenes are sampled along each trajectory at 12-hr intervals, coinciding with the Aqua satellite overpass at ∼01:30 and ∼13:30 local times (LT). When only daytime data are available, samples are only available at ∼13:30 LT. Samples are still included when trajectories advect upwind or downwind out of the regions specified above. ERA-Interim trajectories are used here in order to stay consistent with our prior Lagrangian MCC study (Eastman et al., 2021). A comparison of 10,000 trajectories launched at identical locations, but driven by both ERA Interim and ERA5 showed strong agreement, with 100%, 92%, 89%, and 84% of trajectories remaining within 1-degree of latitude/longitude of one another after 12, 24, 36, and 48 hr, respectively. Additionally, no consistent geographic bias was seen between the ERA5 and ERA Interim trajectories.

2.2. Classifying Types of Mesoscale Cellular Convection

Patterns of mesoscale cellular convection (MCC) are determined using the supervised neural network algorithm introduced in Wood and Hartmann (2006). This routine, as applied and updated in McCoy et al. (2017), analyzes the spatial distribution and quantity of MODIS *Aqua* collection 6.1 liquid water path (LWP, King et al., 2003; Platnick et al., 2015) in scenes from the swath-level, daytime-only satellite data, sampled only at ∼13:30 LT. Each scene is a 256 × 256 km^2 box spaced laterally by 128 km from neighboring box centers, thereby largely overlapping. The classifier determines one of three types of MCC organization: Closed, open, and cellular but disorganized (which maintain some cellular structure, but those structures are not consistent in size and are not consistently repeating). Example classifications are shown in Figure 1 by different colored dots. A visual examination in Eastman et al. (2021) for collection 6.1 classifications in subtropical ocean basins showed an 85%–90%

success rate for the classifier when ~4,000 classified scenes were manually inspected, consistent with the success rate of the algorithm when first developed (Wood & Hartmann, 2006). A sensitivity test was developed here where MCC values were randomized for 10% and then 20% of sampled scenes. Results remained qualitatively consistent when MCC classifications were randomized, though statistical significance was reduced for the 20% randomization test. Scenes are only classified when MODIS cloud top temperatures are within 30K of the ERA5 sea surface temperature. Thus, cloud identifications along trajectories are only for daytime-sampled clouds in the absence of high clouds.

To determine an MCC classification at a trajectory sampling point, all MCC box centers within a 200 km radius of the point are considered. Then the classifier represented over 50% of the time is assigned to the box (e.g., Eastman et al., 2021). This analysis has been repeated using two other schemes for identifying MCC scenes along trajectories: by assigning each sample point the MCC value closest to the point and by assigning each point to the plurality of all MCC types within 200 km. Results were qualitatively unchanged regardless of which scheme was employed. If an MCC sampling scheme fails to produce an MCC classification, then that sample is excluded from the analysis.

This study compares MCC transitions that occur over 24 hr, from ~13:30 to ~13:30 LT on the following day. To compare MCC transitions that may occur at varied times across our set of Lagrangian trajectories, we re-define trajectory times relative to the time that a transition between MCC types occurs. For example, take a trajectory that undergoes a transition from closed-to-open MCC over ~24 hr. At the start of the transition, a closed MCC scene is observed by *Aqua* at 13:30 (LT) and assigned to the transition sample time $t = -24\ hr$. At the end of the transition, after 24 hr have elapsed, the cloud scene is now identified as open MCC by the neural network and the sample time is $t = 0\ hr$. All other points along this trajectory now exist relative to this new transition-relative timeline. This study only analyzes transitions that occur over subsequent Aqua observations spaced roughly 24 hr apart. The actual temporal spacing may be closer to 25 hr since the trajectories are advecting westward, extending the time between subsequent sunrises. If a transition is seen over 48 hr with a missing observation in the middle, it is not included since that missing observation could have the MCC structure of the 0-hr *or* the 48-hr classification, making any associated data ambiguous.

Three types of mesoscale morphological cloud transitions are compared in this study: closed-to-closed MCC (i.e., no transition, C-C), closed-to-open MCC (C-O), and closed-to-disorganized MCC (C-D). As in Eastman et al. (2021), we include C-C cases as a baseline comparison for the transitioning cases. Requiring closed cell MCC observations to be present at time $t = -24\ hr$ and another closed, open, or disorganized MCC observation at $t = 0\ hr$ caused a significant number of our trajectories to be excluded from this study. The total number of contributing trajectories, which observe any MCC change from closed cell at hour $t = -24\ hr$ to open, closed, or disorganized at hour $t = 0\ hr$ is 33,000. Heat maps are shown in Figure 2, where red, blue, and orange contours represent the number of closed-open trajectories, closed-closed trajectories, and closed-disorganized trajectories, respectively, per five-degree latitude-longitude grid box. The location of each trajectory is assigned to the midpoint of each 24-hr transition, at $t = -12\ hr$. Maxima in the geographic distributions are shown as "+" symbols. Also shown in grayscale is the total number of trajectories that observe any MCC transition from closed cell (C-O, C-C, or C-D). The contours in Figure 2 shows that the geographical distributions of C-O and C-D trajectories tend to favor offshore, downwind locations relative to C-C trajectories. The SE Pacific contains the largest proportion of trajectories studied here, though the NE Pacific and SE Atlantic are major contributors, while the E Indian sees far fewer transitions from closed cell MCC. Black boxes on Figure 2 show the regions that contain all trajectory launch points.

Prior work (Eastman et al., 2021) examined the average evolution of cloud cover for the C-C, C-O, and C-D transitions for times $t = -24$, $t = -12$, and $t = 0$ hr. Results there show that scenes tend to remain overcast from $t = -24$ to $t = -12\ hr$, then breakup between $t = -12$ and $t = 0\ hr$. This suggests that the vast majority of transitioning trajectories studied here are changing between 1:30 and 13:30 local time, in the morning. This is consistent with the results of Wood et al. (2008), where open cells were observed to form in the early morning. Consistent overcast conditions at $t = -24$ and $t = -12\ hr$ reduces potential biases associated with differing cloud amounts affecting retrieved cloud properties. Basically, this implies that comparisons between trajectories at $t = -24$ and $t = -12\ hr$ are "apples-to-apples" with respect to cloud cover, since most scenes are overcast.

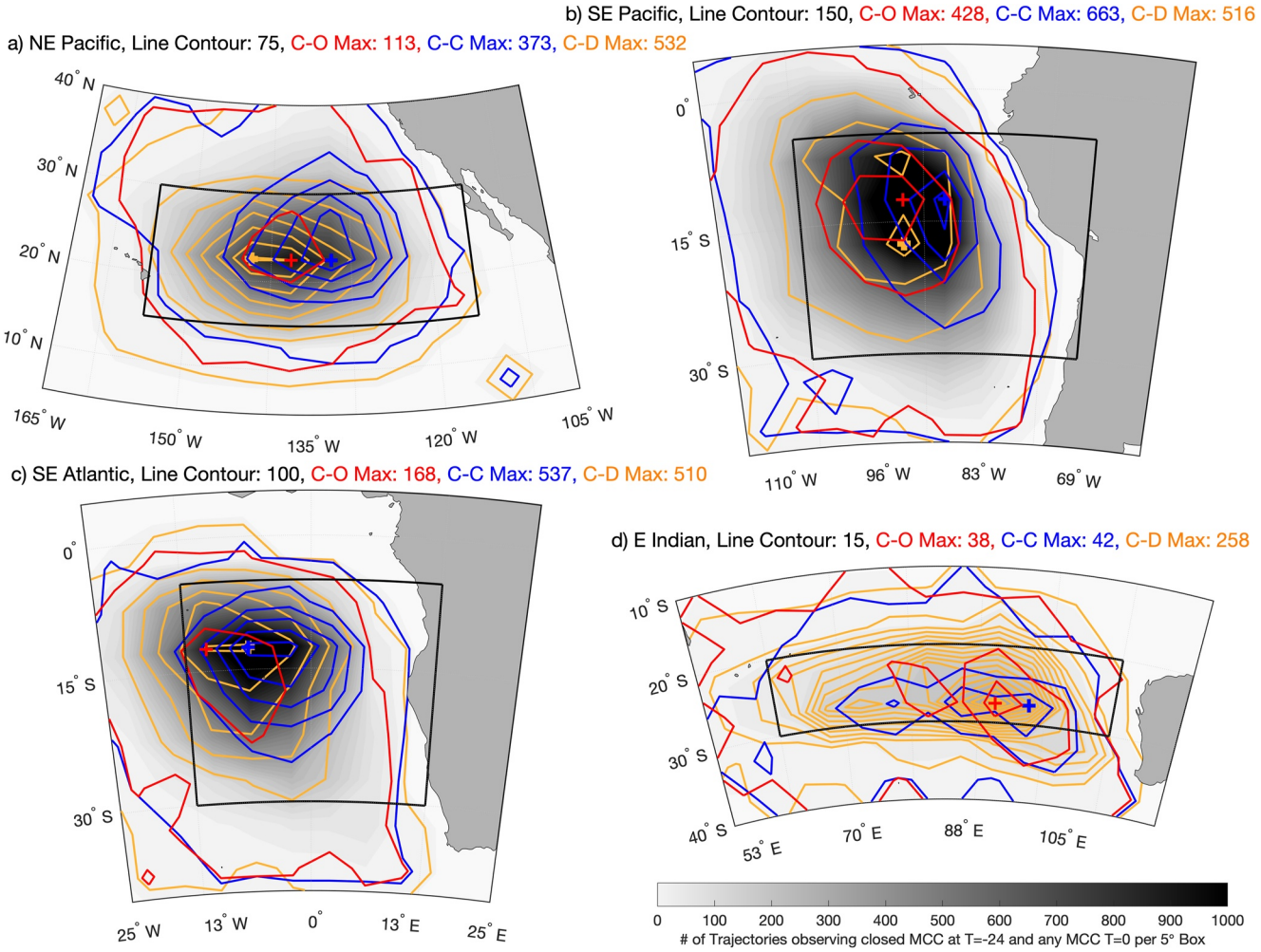

Figure 2. Heat maps showing the number of 24-hr trajectory midpoints (defined as the location at $t = -12$ for trajectories that transition starting at $t = -24$ and ending at $t = 0$) per 5-degree latitude/longitude grid box. Red (C-O), blue (C-C), and orange (C-D) contours vary between frames, with the contour interval listed in each frame subtitle. Maxima are shown by red, blue, and orange "+" signs. Gray contours represent the number of trajectories in the analysis that show any of the three transitions (C-O, C-C, and C-D), using the same contour interval (shown in frame D) within each frame. Regions where trajectories originate (at hr 0 from hr −48 to +48) are shown by black boxes in the centers of the maps.

2.3. Meteorological and Cloud Variables

Meteorological data are provided by 6-hourly ERA5 reanalysis (Copernicus, 2017) grids interpolated to match the Aqua satellite sample times at 01:30 and 13:30 LT. Data are generated by ECMWF on a 1° × 1° latitude/longitude grid. Samples along trajectories include all 1° × 1° grid box centers that fall within a 100 km radius from each trajectory sampling point.

Observational data used here include cloud cover from MODIS C6.1 L3 cloud mask for day and night (Hubanks et al., 2008; Oreopoulos, 2005) and day and night AMSR/E cloud liquid water path (CLWP, Wentz & Meissner, 2004) adjusted for rain water content as in Eastman et al. (2021) and divided by MODIS cloud cover to only represent cloudy portions of samples. Daytime-only droplet number concentration (N_d) is derived from MODIS cloud droplet effective radius and MODIS CLWP (King et al., 2003), computed as in Possner et al. (2020) using relationships determined by Boers et al. (2006) and Bennartz (2007). Day and night rain rate data (Eastman et al., 2019) come from AMSR/E 89 GHz brightness temperatures (Ashcroft & Wentz, 2019) tuned using CloudSat rain-profile rain rates (Lebsock & L'Ecuyer, 2011) and ERA5 sea surface temperature (SST), ERA5 10-m wind speed, and AMSR/E column integrated water vapor (Wentz & Meissner, 2004). The depth of the planetary boundary layer (PBL) is estimated for day and night using the difference between the SST and cloud top temperature (CTT), where the CTT representative of the cloud top is determined using a training

Table 1
A List of all Variables Tested as Predictors of MCC Transitions in This Study, Along With Their Standard Deviation (σ), Units, and the Source of the Data

Predictor variable (name, level, abbreviation)	σ	Units	Source
Subsidence (700 hPa, ω)	0.0963	Pa s^{-1}	ERA5
Sea Surface Temperature (SST)	0.699	K	ERA5
Cloud Only LWP (CLWP)	0.0413	kg/m^2	AMSR/E (LWP) & MODIS (CC)
Specific Humidity (700 hPa, q)	0.00157	kg/kg	ERA5
Relative Humidity (1000 hPa, RH)	7.26	%	ERA5
Lower Tropospheric Stability (θ_{700}–θ_{1000}, LTS)	2.26	K	ERA5
Planetary Boundary Layer Depth (PBL)	0.557	Km	MODIS & CALIPSO
Rain Rate	0.0525	mm hr^{-1}	AMSR/E 89 GHz T_b & CloudSat
Wind Speed (wsp, 10m)	2.07	m s^{-1}	ERA5
Cloud Droplet Number Concentration (Nd)	46.6	cm^{-3}	MODIS
Latent Heat Flux (LHF)	50.9	W m^{-2}	ERA5
Sensible Heat Flux (SHF)	11.7	W m^{-2}	ERA5
Wind Shear (700–925 hPa)	3.58	m s^{-1}	ERA5
Wind Shear (925–1000 hPa)	1.06	m s^{-1}	ERA5
Divergence (1000 hPa)	8.36E−06	s^{-1}	ERA5
Divergence (925 hPa)	7.72E−06	s^{-1}	ERA5

data set from CALIPSO Vertical Feature Mask (VFM, v4, Vaughan et al., 2004) and the routine introduced in Eastman et al. (2016). This routine estimates the fraction of cloud cover at PBL top as a function of cloud amount.

Variables in this study are converted to anomalies relative to their seasonal and diurnal cycles within 1° × 1° latitude/longitude grid boxes by subtracting a 100-day running mean centered on each day within each grid box. This improves comparability for trajectories that may occur in different regions or different seasons. To allow for the direct comparison of several predictor variables that have differing units, all anomalies have been standardized (divided by the standard deviation of the entire sampled population, σ). All variables used as predictors are listed in Table 1 along with their σ values, units, and sources.

The presence of overlying supercooled liquids or ice clouds may cause biases in some of our observed predictor variables. A filter has been applied to this analysis using MODIS Aqua L3 1° × 1° pixel counts for cloud cover at and above 640 hPa. This filter excludes all observations where clouds at and above (in altitude) 640 hPa are observed. Results were qualitatively unchanged by the application of this filter, so we conclude that the presence of high clouds is not likely biasing results in this work by altering radiative balance at cloud top. The exclusion of high clouds does remove all cases where MCC transitions take place under an overlying middle or high cloud deck, so the effects of overlying clouds cannot be assessed here, though overlying clouds could potentially modify transitions.

3. Results

3.1. Composite Trajectories

The mean locations of trajectories composited by MCC transition type are compared in Figure 3 for each region along with the composite sea level pressure (SLP) and lower tropospheric stability (LTS, θ_{700}–θ_{1000}) fields (these are raw values, not standardized as in the later portion of this study). Data fields are composited based on values at trajectory hour $t = 0$ *hr* (the afternoon after the transition) for each transition type. Trajectory composites for the three separate transition types are plotted in frames i–l to better compare their relative spatial evolutions. Composite maps for all transition types show similar weather patterns and trajectory locations, but subtle differences are apparent. In all regions but the E. Indian, the C-O transition coincides with a significantly stronger subtropical high-pressure center (a comparison of standard error bounds shows significant differences in the mean values),

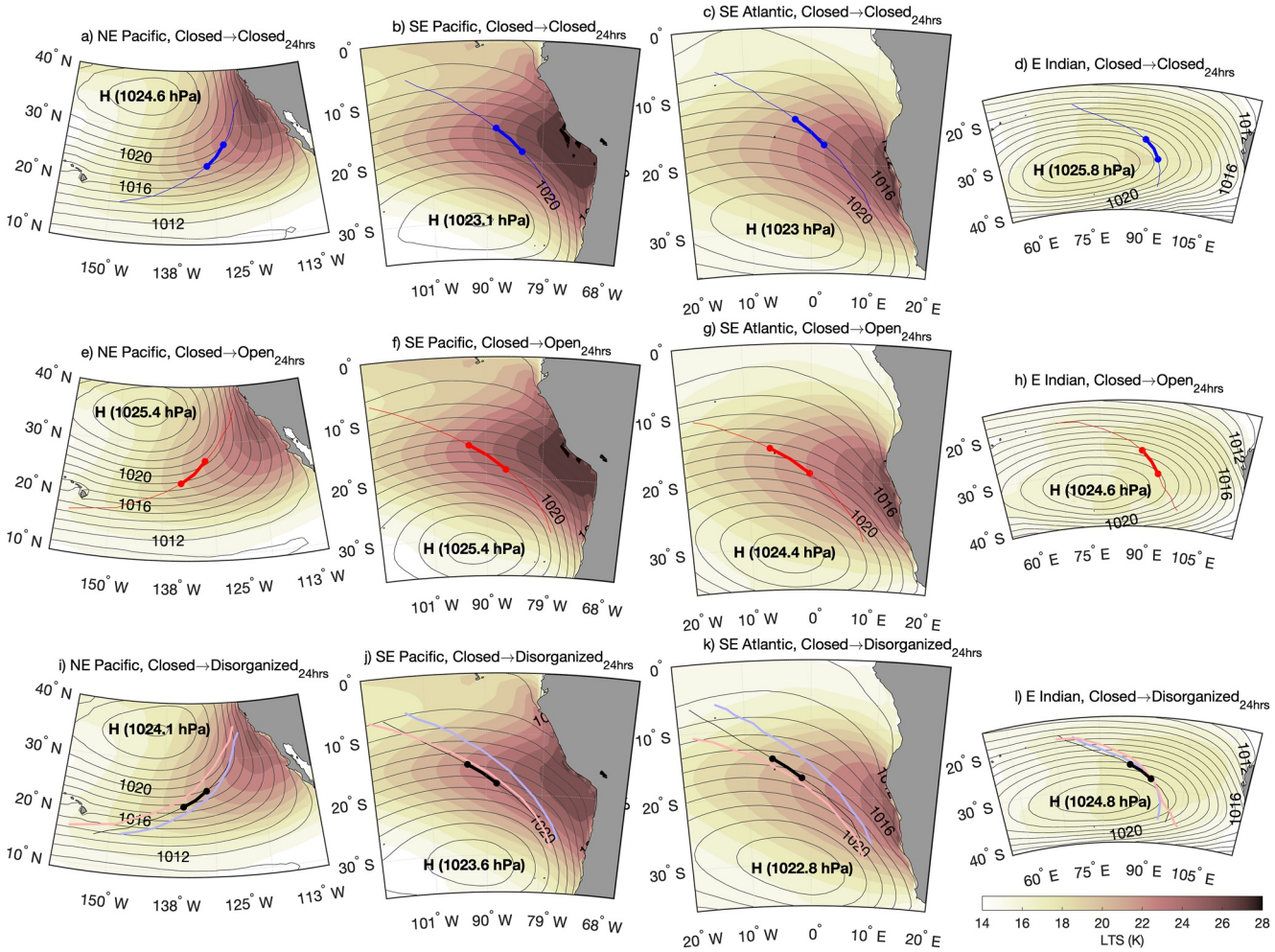

Figure 3. Composite mean Lagrangian trajectories from $t = -72$ to $t = 72$ hr, sea level pressure fields (lines), and lower tropospheric stability fields (shading), for all three MCC cloud transition types: closed-closed (blue, a–d), closed-open (red, e–h), and closed-disorganized (black, i–l), in all four study regions. Fields are composited based on values at $t = 0$ hr. Highlighted portions of the curves (thick line between dots) indicate the mean location of the specified transition. Trajectory composites for the three separate transition types are plotted together in frames (i–l) with their respective colors for comparison.

with isobars spaced closer together. Inversion strength, measured by LTS, is stronger for the C-C and C-O sets. The C-C trajectories are, on average, closer to the eastern, upwind portion of the regions, while the C-O and C-D sets tend to occur slightly further offshore.

3.2. Examining Variable Predictive Power in Lagrangian Mesoscale Cloud Morphology Transitions

To assess the power of a variable in predicting a Lagrangian transition between MCC types, we develop a novel methodology that assesses both the variable magnitude and the lead-time necessary for predictive skill. This is an improvement from Eastman et al., 2021, which employed a composite analysis that only showed whether mean values of predictors were significantly different between trajectory sets, and only for 12 and 24-hr lead times. Here, we use 10-m wind speed as a predictive variable to demonstrate this new method in Figure 4. Trajectory sets that exhibit a specific transition (e.g., C-O) are binned by the value of the predictor, x, at a chosen lead-time, t, in eight fixed-width bins along x. Figure 4a shows the number of trajectories that undergo either C-C or C-O transitions in bins of standardized wind speed anomaly for the chosen lead time, $t = -24$ *hr*. In this case, we see that the number of C-O trajectories that transition from $t = -24$ to $t = 0$ *hr* increases when wind speed is anomalously strong at lead-time $t = -24$ *hr* while the number of C-C trajectories varies little with wind speed. Figure 4b shows the fraction of C-O trajectories relative to the sum of C-O and C-C trajectories per wind speed bin based on the curves in Figure 4a (red curve over red + blue curves). In Figure 4c, this fractional calculation

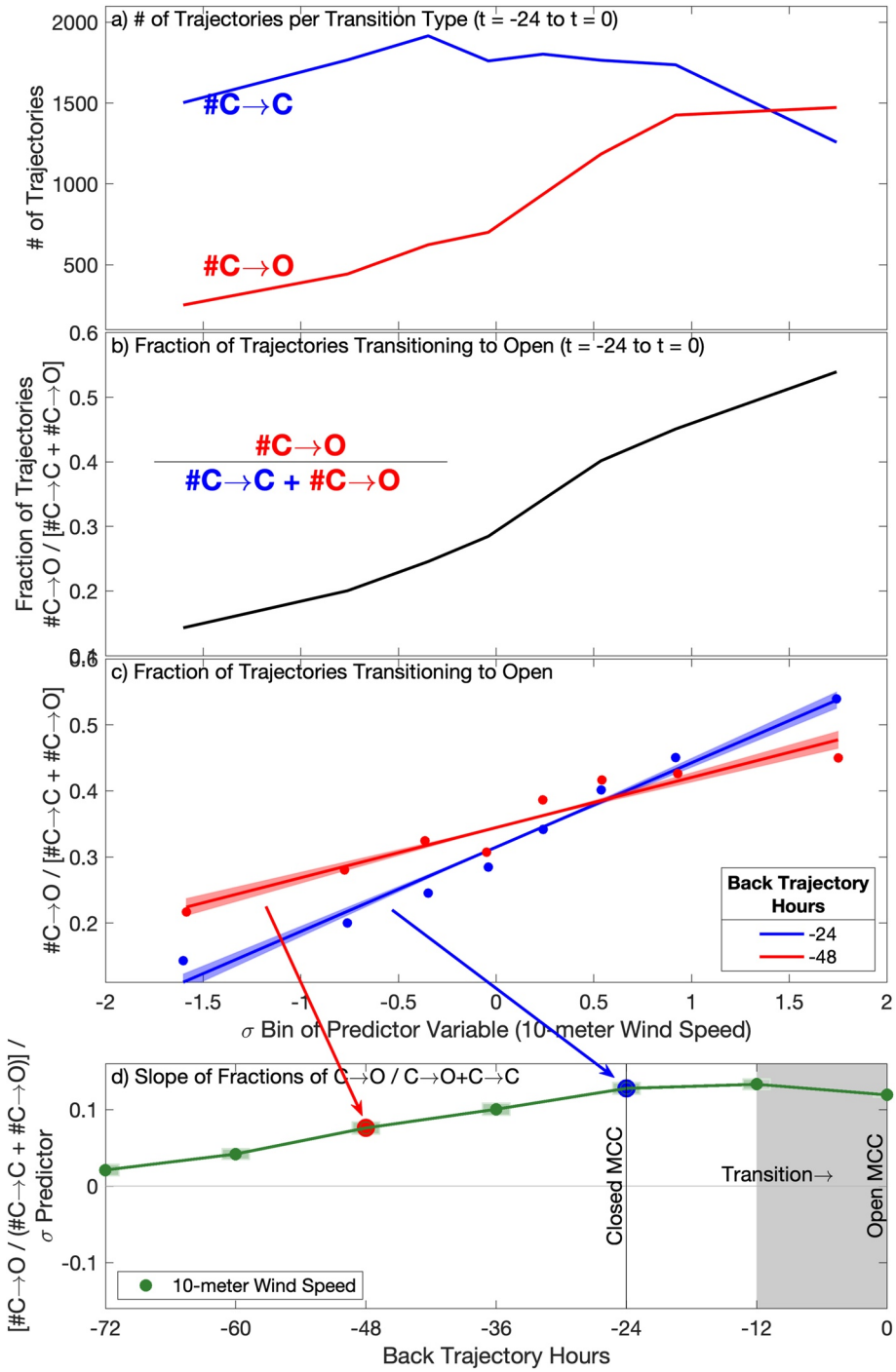

Figure 4. (a) The number of trajectories that transition from closed-to-open (red) mesoscale cellular convective (MCC) or remain closed MCC (blue) from $t = -24$ to $t = 0$ hr for bins of wind speed anomaly observed at lead-time $t = -24$ hr. (b) The fraction of trajectories that transition from closed-to-open MCC relative to the number of trajectories that either show the closed-open transition or remain closed MCC from $t = -24$ to $t = 0$ hr for bins of wind speed anomaly at lead-time $t = -24$ hr. (c) The fraction of closed-to-open transitions from $t = -24$ to $t = 0$ hr as in (b), but for wind speed anomaly bins at lead-time of $t = -24$ (blue, same as black line in (b) and $t = -48$ hr (red) with linear best fits. (d) Slopes of the linear best fits as in (c) for predictor variable (wind speed) lead times between $t = -72$ and $t = 0$ hr. Wind speed, the predictor variable, is standardized. Error bounds are calculated using the standard deviation of the slope as in Warren et al. (2007), and are represented by red and blue shaded regions surrounding the lines in frame c and the shading surrounding the green points in frame (d).

for C-O transitions is repeated for the predictor variable at lead time $t = -48$ *hr* and compared with the C-O fraction at lead time $t = -24$ *hr* from Figure 4b. Best fit lines are applied to each C-O fraction and tested for significance at 95% confidence. Additionally, error bounds calculated as standard deviations of slopes, as in Warren et al. (2007), are shown as shaded regions surrounding the lines both here and for all future linear fits to scatter plots. The resulting slopes of these lines, which are both significant at 95% confidence, are plotted versus their respective lead times in Figure 4d. Slopes are computed similarly at 12-hr intervals for all lead-times from $t = -72$ to $t = 0$ *hr* and are plotted, here and in subsequent figures, *only if the slopes are significantly different from 0 at the 95% confidence level*. If a slope is not significant at this level, the point is excluded from the analysis and the predictor is not considered to have a significant effect on an MCC transition. Error bounds are shown by shaded regions at each point. Error bounds only represent error in the *y* direction. In this case, we find that wind speed is significantly associated with the C-O transition at lead times of at least 72 hr but that wind is a stronger predictor at shorter lead times (Figure 2d).

To put Figure 4 and this methodology in context, we analyze a "perfect predictor" case. We create a fictitious predictor variable to describe a C-O transition where the variable is normally distributed around 0. For any variable value below zero, we assume all associated trajectories remain closed cell MCC for 24 hr. For variable values greater than zero, all associated trajectories transition from closed to open cell MCC. When analyzed as in Figure 4, we find that this "perfect predictor" generated a slope of $m = 0.42$ at lead time $t = -24$ *hr*. Thus, the highest attainable slope that can occur in this analysis is 0.42, which is ∼3x larger than the wind speed case ($m = 0.13$ at lead time $t = -24$ *hr*, Figure 4d). This is shown in supplemental Figure S1 in Supporting Information S1, along with the line fit to the 24-hr wind speed predictor analysis from Figure 4c (blue line in 4c). The "perfect predictor" slope is sensitive to the number of bins used along x, with slopes ranging between 0.43 and 0.4 for bin amounts between eight and 100. For this slope analysis, eight bins are always used along x.

We apply the above methodology to a suite of predictors in Figure 5, contrasting their power in predicting C-O (5a) versus C-D (5b) transitions. Consistent with Eastman et al. (2021), Figure 5 shows that strong wind, more intense rainfall, increased CLWP, and decreased N_d are associated with C-O transitions. In contrast, the C-D transitions are preceded by warmer SST, weaker LTS, lower $q_{700,}$ weaker subsidence, less CLWP, and deeper PBLs. The relationship between the analyzed variables in Figure 5b (the C-D transition) suggests an entrainment-driven warming and drying of the cloud deck as it transitions from closed MCC to disorganized, previously hypothesized in Eastman et al. (2021). This mechanism is similar to the SST-driven warming, deepening, and decoupling process described in Wyant et al. (1997) except that here the PBL deepening is associated with a drier free troposphere and weaker subsidence in addition to the warming sea surface. The role of weakening subsidence in the "canonical" Sc-Cu transition was also shown by Sandu et al. (2010) and Sandu and Stevens (2011).

Figure 5 expands upon the conclusions from Eastman et al., 2021 by showing the relative power of these variables to predict an MCC transition, as well as showing the different timescales associated with different variables. The C-O transition is most powerfully predicted by more intense rain, low N_d, and strong wind. The expanded timescale view here shows that while precipitation and N_d may act on the transition over the course of a single diurnal cycle, wind speed is markedly stronger for C-O transitions for several days prior to the transition. A similar distinction is seen for the C-D transition: A warm SST precedes the C-D transition for several days, while entrainment related processes such as a deep PBL, reduced CLWP, declining subsidence, and a drying free troposphere appear to act on a shorter, diurnal timescale. This hints at a situation where processes act quickly to modify the clouds, but these processes may be anchored to distinct regimes (warm SST for the C-D transition, and windy for the C-O) that favor one process over the other.

Figure 5 represents all four study regions combined, as shown here, but has also been produced for each individual ocean basin. As in Eastman et al. (2021), results are qualitatively similar for all four ocean basins studied, though additional noise and uncertainty is present in the relatively poorly sampled East Indian basin, where the C-D transition shows less contrast with the C-O transition.

3.3. Relative Importance of Wind and Rain in Initiating the Lagrangian Closed to Open MCC Transition

Eastman et al. (2021) queried whether there was a relationship between wind and rain or whether the two variables acted independently to drive the C-O transitions. We explore this question in Figure 6a, testing whether wind

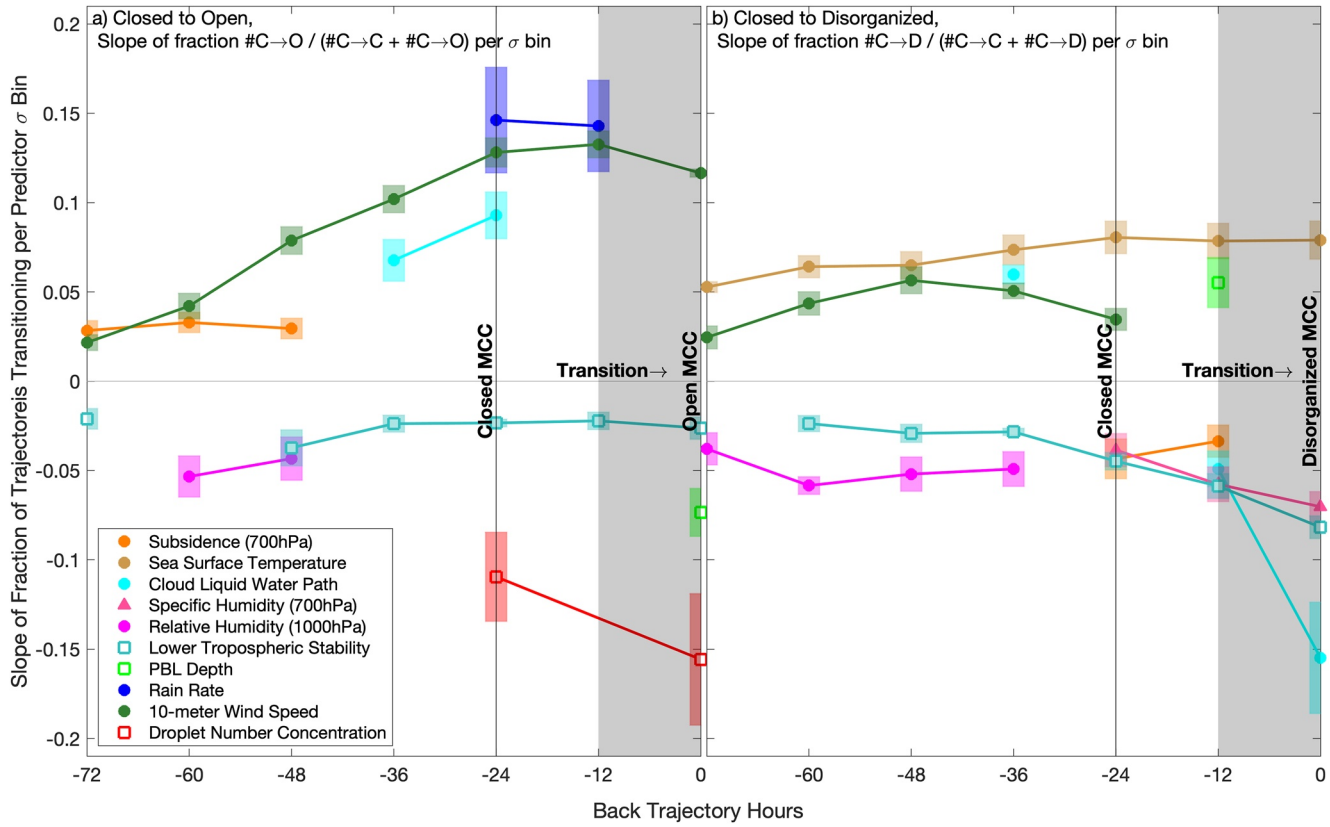

Figure 5. Variables tested as predictors (as in Figure 4) of (a) the closed-to-open mesoscale cellular convective (MCC) transitions and (b) the closed-to-disorganized MCC transitions, showing the fraction of trajectories that exhibit the specified transition relative to the sum of trajectories that do transition or do not transition, for variable predictor lead times. Variables in the legend that do not appear on the plot were tested, but showed no significance as a predictor of a transition.

speed drives C-O transitions through enhanced surface fluxes (which could drive enhanced rainfall) or through other wind-related, mechanical properties such as shear or convergence. An analysis similar to that in Figure 5 is performed in Figure 6a, where we compare sensible and latent heat fluxes (SHF and LHF, respectively), with wind shear within the PBL (magnitude of the vector difference between 1,000 hPa and 925 hPa) and shear across the trade inversion (magnitude of the vector difference between 925 hPa and 700 hPa), and with convergence at 1,000 hPa and at ~ cloud level (925 hPa).

It is apparent from Figure 6a that increased LHF into the PBL from the sea surface is a significantly stronger predictor of C-O transitions than any other variable except for wind speed itself, which is, curiously, a stronger predictor than LHF. Shear and convergence/divergence show insignificant predicting power, so are rejected as major predictors of the C-O transition. To establish a clearer picture of the relationship between winds, fluxes, and the C-O transition and to attempt to learn why wind speed is a stronger predictor of the transition than LHF, we further expand this analysis by subsetting trajectories by their mean LHF. Two trajectory sets are created based on the mean trajectory LHF for all hours prior to and including $t = 0\ hr$: an anomalously weak LHF set (Figure 6b) and an anomalously strong LHF set (Figure 6c). These sets are segregated based on whether the mean LHF anomaly for all times along each trajectory is above or below 0. All predictor variables from Figures 5 and 6 were tested for these subsets, but only variables showing significant differences between sets are plotted. When LHF is weak (Figure 6b), wind speed remains a strong predictor of C-O transitions. In this case, relative humidity at 1,000 hPa is nearly equivalent in strength to wind speed and rain rate in predicting C-O transitions. Convergence of surface winds may also play a minor role in the C-O transitions under weak LHF conditions, possibly by driving increased rainfall. When LHF is high (Figure 6c), wind speed and rain rate along with LHF are strong predictors of the transition.

We conclude from Figure 6 that C-O transitions occur when moisture flux or content in the PBL are anomalously high. Further, excesses in moisture flux and content both appear to be linked to strong wind speed. When LHF

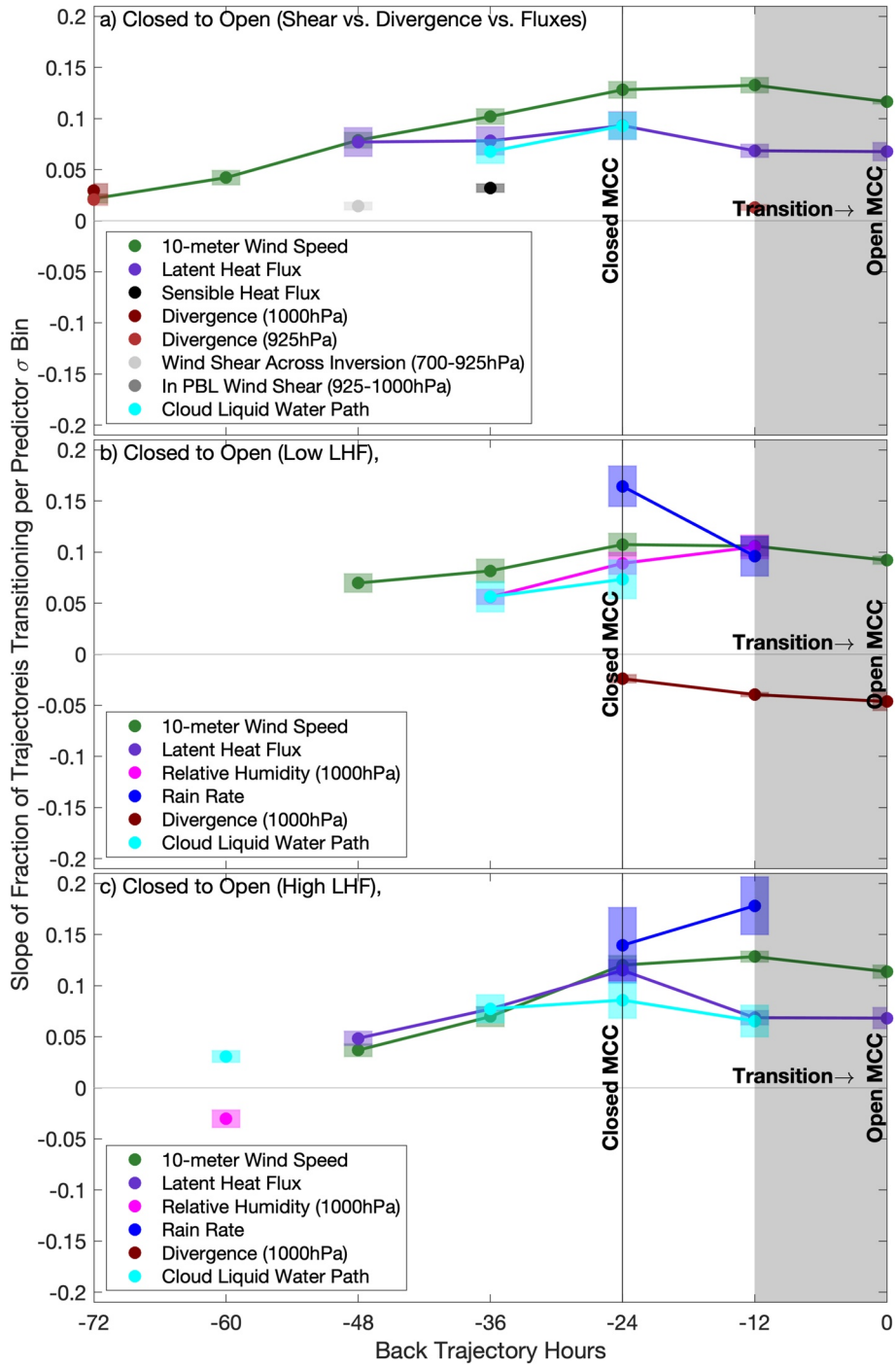

Figure 6. (a) Wind and flux variables tested as predictors of closed-to-open mesoscale cellular convective (MCC) transitions for variable lead times (as in Figures 4 and 5). (b) Wind, humidity, and flux variables tested as predictors of closed-to-open MCC transitions for a subset of trajectories with anomalously low mean latent heat fluxes (LHF). (c) As in (b), but for anomalously high mean LHF.

is anomalously *low*, wind speed anomalies behave similarly to PBL moisture *content* (RH_{1000}) anomalies as a predictor of C-O transitions. When LHF is anomalously *high*, the effect of wind speed appears similar to PBL moisture *flux* anomalies. This can be loosely quantified by rearranging the relationship $\boldsymbol{LHF' \propto wind'/RH'}$ to $\boldsymbol{wind' \propto LHF' \times RH'}$, where strong wind anomalies (wind') guarantee either high moisture flux (LHF') or high moisture content (RH') in the capped PBL. This brings about a conceptual source-sink model where an increase

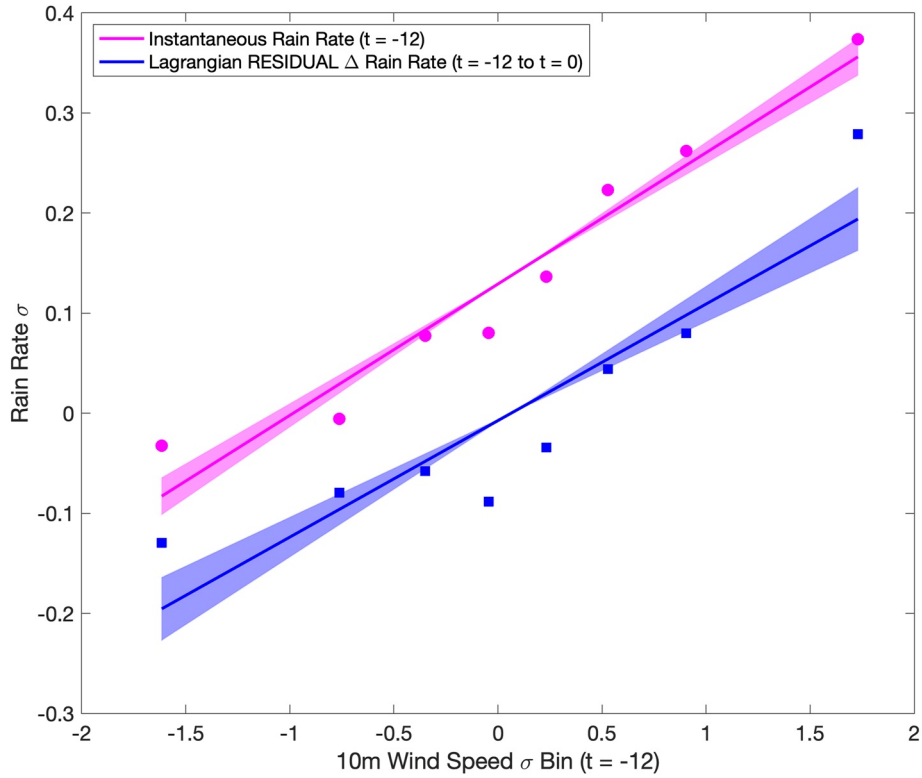

Figure 7. Mean rain rate anomalies (magenta) and 12-hr residual Δrain rate anomalies (blue) from the CloudSat-tuned AMSR/E 89 GHz brightness temperature rain rate estimates for bins of constant wind speed anomalies. Analysis for closed cell mesoscale cellular convective with CC>90% only at lead times $t = -12$ and $t = 0$ hr. All variables standardized. Both slopes are significant at the 99% level.

in moisture source through wind-driven flux and content could be partially balanced by an increase in precipitation, acting as a compensating moisture sink. A simpler mechanistic interpretation, tying wind speed directly to LHF, fails to account for the stronger relationship seen between wind speed and the C-O transition compared to LHF (as seen in Figure 6a). Inclusion of RH in addition to LHF and wind speed more completely captures the relationship behaviors seen in Figure 6.

To further establish a link between wind and precipitation in closed cells, we test wind speed as a predictor of rain rate using our Lagrangian framework. In Figure 7, we examine a set of trajectories that are classified as closed cells at $t = -24$ *hr* that remain overcast (CC>90%) overnight at $t = -12$ *hr* and into the next day at $t = 0$ *hrs*. When wind speed, binned along x, is strong at $t = -12$ *hr*, concurrently observed rain rates (magenta points in Figure 7) are higher. Rain rates also tend to increase in the 12 hr after strong winds are observed ($t = -12$ to $t = 0$ *hr*, blue points in Figure 7). Figure 7 shows the residual Δrain rate, which is defined as the change observed after taking into account the tendency of a variable to regress toward a mean state (i.e., diminishing the initial anomaly, Eastman & Wood, 2016; Eastman et al., 2016). Figure 7 shows a link between wind speed and rain rate, where stronger wind is associated with more intense rain rates, and with anomalously increasing rain rates over the 12 hr following the strong wind observation.

The mechanism proposed here (*wind'* $\propto$ *LHF'* $\times$ *RH'*) posits that wind speed is a variable whose influence is comparable to the combination of moisture flux and moisture content in shallow, capped, marine boundary layers. To further demonstrate this, we can expand the relationship from the rearranged latent heat equation and from Figure 7 by assuming moisture flux and moisture content are functions of wind speed. Equation 1 describes a relationship where a change in rain driven by wind speed would be roughly equivalent to the sum of changes in rain produced by changing moisture flux and changing moisture content, both driven by changes in wind speed.

$$\frac{d\Delta\text{Rain}}{d\text{Wind}} \approx \frac{\partial\Delta\text{Rain}}{\partial LHF}\frac{dLHF}{d\text{Wind}} + \frac{\partial\Delta\text{Rain}}{\partial RH}\frac{dRH}{d\text{Wind}} \quad (1)$$

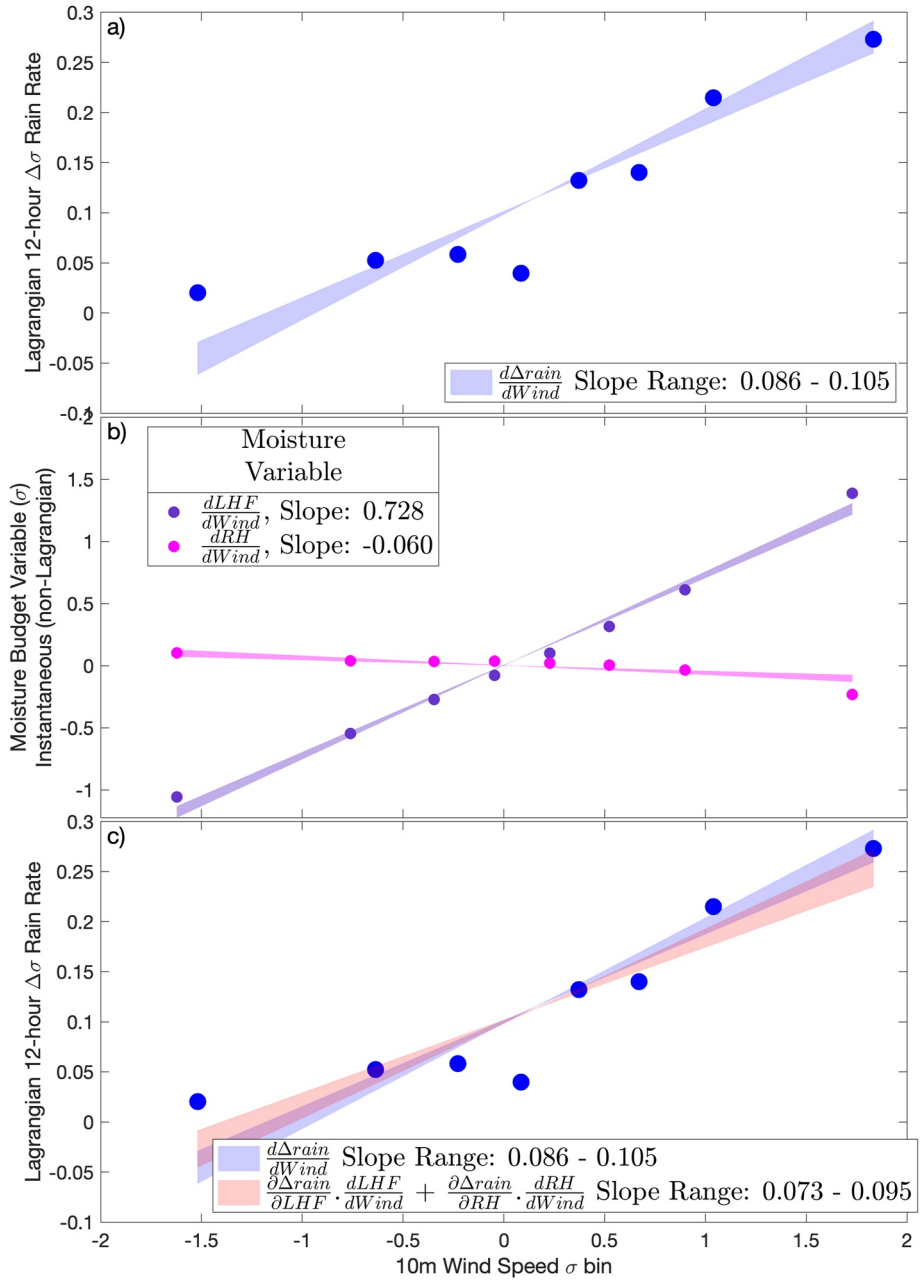

Figure 8. (a) The 12-hr Lagrangian rain rate change observed as a function of initial wind speed anomaly. Confidence bounds are shown by the blue shading, with the possible range of slopes shown in the legend. (b) The instantaneous values of RH_{1000} and latent heat fluxes as a function of wind speed. (c) The points and confidence bounds from frame (a) (in blue) and the slope and confidence bounds determined from Equation 1 (in red). Overlap in the confidence bounds suggests that these relationships are similar. Data shown for closed cell mesoscale cellular convective only with CC>90%.

Each element of the system in Equation 1 can be tested using our Lagrangian framework, as presented in Figure 8. As in Figures 7, Figure 8 shows data for overcast (CC>90%) closed cell MCC environments. The 12-hr Lagrangian change in standardized rain rate as a function of initial wind speed ($\frac{d\Delta\text{Rain}}{d\text{Wind}}$) is well described by a linear fit, with slopes ranging between 0.086 and 0.105 at 95% confidence (Figure 8a). The instantaneous perturbations in LHF and RH as a function of wind speed ($\frac{dLHF}{d\text{Wind}}$, $\frac{dRH}{d\text{Wind}}$) have slopes of 0.728 and −0.060, respectively (Figure 8b). Due to their strong interdependence, the 12-hr Lagrangian changes in rain as a function of LHF and RH_{1000} were determined using a multiple linear regression ($\frac{\partial\Delta\text{Rain}}{\partial LHF}=0.120$, $\frac{\partial\Delta\text{Rain}}{\partial RH}=0.061$). Using these observationally determined slopes, we calculate the value of the right-hand side of Equation 1 to have a range between 0.073

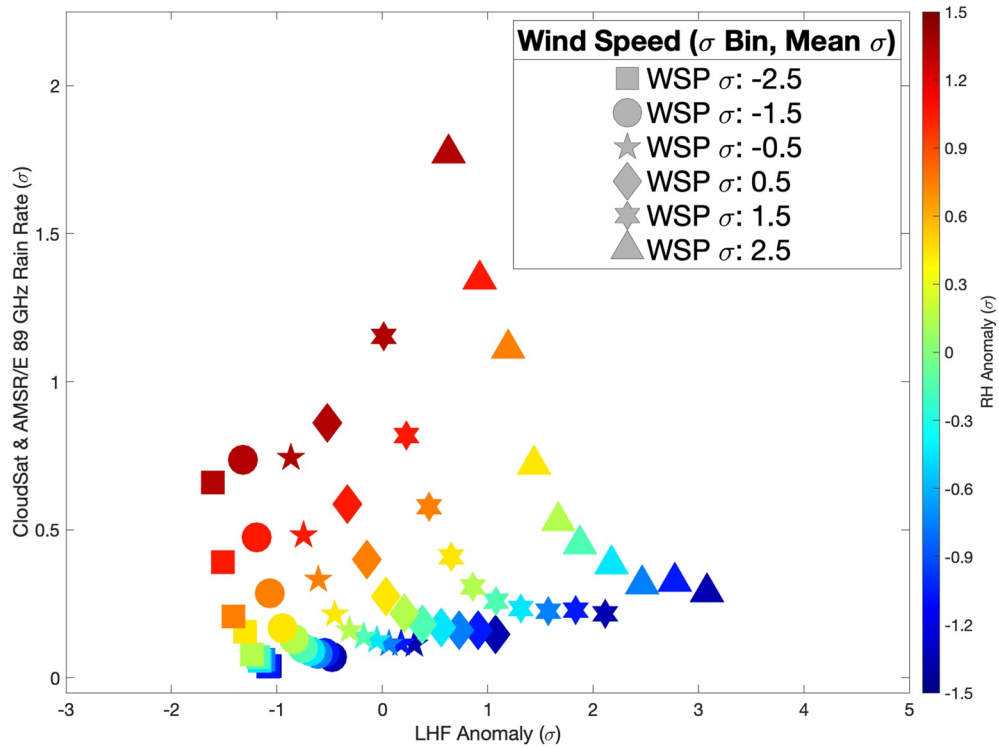

Figure 9. Rain rate (*y* axis) as a function of latent heat fluxes anomaly (*x* axis) for overcast (CC>90%) scenes within 1° × 1° grid boxes. Data are grouped by wind speed anomaly σ bin, shown by shape and defined in the legend. Data within each wind speed bin are divided into RH_{1000} bins (RH_{1000} bin bounds are the same for every wind speed σ bin), and each point represents an RH_{1000} bin within a wind speed bin. RH_{1000} values are shown in color.

and 0.095 (shown in Figure 8c as the red range). The range from 8a is shown again in 8c in blue for comparison. The two ranges fall within each other's confidence bounds, showing a high degree of equivalence between the two sides of this equation. This validation of Equation 1 shows that, at least according to ERA5, the change in satellite-observed rainfall produced by a wind speed perturbation is roughly equivalent to the change in rain rate forced by the moisture variable perturbations associated with that wind speed perturbation.

Results thus far indicate a complex, but significant, relationship between rain rate, wind speed, RH_{1000}, and LHF. This relationship is better visualized in Figure 9, where all four variables are represented in a single plot. This 4-dimensional plot is showing relationships in an Eulerian framework for data in 1° × 1° grid boxes for years 2007–2010 for boxes with cloud cover greater than 90%. In Figure 9, symbols represent a set of grid boxes for a wind speed anomaly σ bin; therefore, for example, triangles indicate a set of observations that are anomalously windy. For data within each wind speed bin, data points are separated into bins determined by the RH_{1000} anomaly, represented by symbol color. These colored symbols are then plotted on an *x*-*y* axis where their mean LHF values are shown along the *x* axis and their mean rain rates (not anomalies, but σ values above 0) are shown along y. With this plot, a reader can hold any single variable constant, either by keeping constant color, constant shape, or constant value along an axis. In doing so, the reader can see how these variables change relative to one another. Most relevant to this study, Figure 9 shows that for a constant LHF value (holding x constant), an increase in rain rate (looking up in y) is associated with stronger wind speed and higher RH_{1000}. Figure 9 also shows that for a constant RH_{1000} (holding color constant), an increase in wind speed (changing symbols from left to right) is associated with more LHF and more intense rain. The take home message of Figure 9 is that stronger wind speed is associated with a greater overall sum of moisture flux and moisture content, and an increase in rain rate.

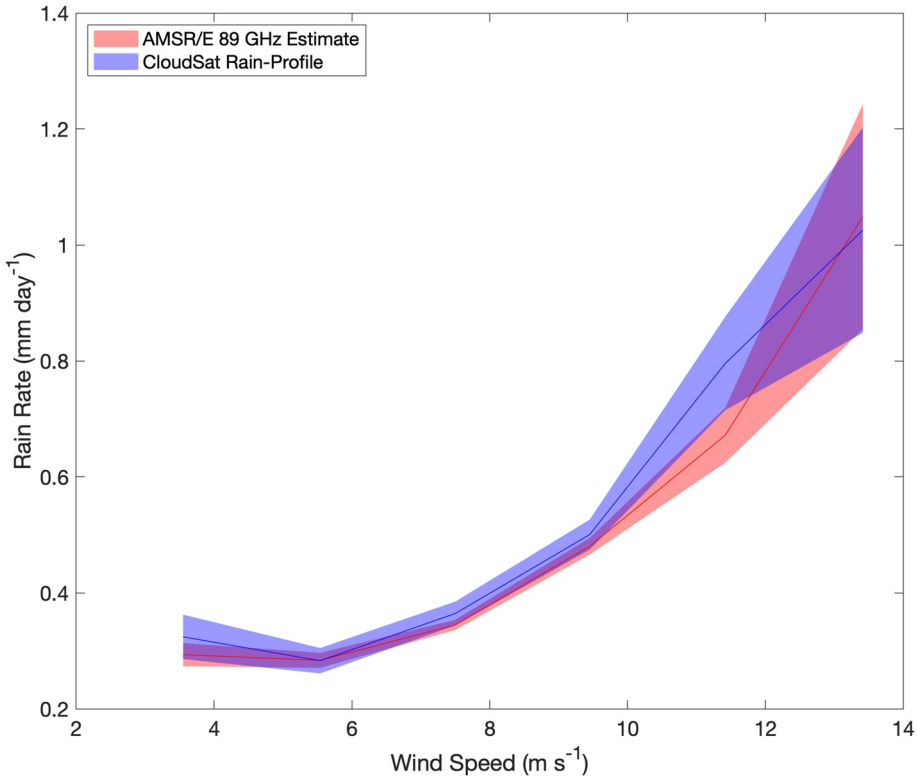

Figure 10. A comparison of CloudSat rain-profile rain rates to AMSR/E 89 GHz T_b-derived rain rate estimates for equivalent bins of wind speed. Data are for all available overlapping 100 km radius samples taken along our trajectories where an mesoscale cellular convective classification was assigned. Shaded regions show the standard error of the mean for each wind speed bin along x.

4. Validation, Context, and Limitations of Results

4.1. Ensuring Validity of Results

One possible issue with the prior analyses is the mutual association of warm microwave brightness temperature (T_b) with strong wind speed and a more intense rain rate. This is shown and accounted for in the binning routine introduced in Eastman et al. (2019), which describes the precipitation product used here. However, to independently verify that more intense rain rates are in reality associated with stronger winds, and to apply the relationship more generally to all three of our MCC types, we compare ERA5 wind speeds to CloudSat rain-profile surface rain rates and AMSR/E 89 GHz rain rate estimates (Figure 10). The CloudSat rain rate versus wind speed relationship is nearly identical to that seen for AMSR/E rain rates for co-located observations for all available scenes classified by the MCC classifier. This suggests that the signal in rain rate seen by the CloudSat tuned AMSR/E rain rate product is not likely an artifact produced by co-located strong winds.

Another possible issue with the rain-wind results presented here is the reliance, thus far, on rain rate as the only response variable studied. In order to lend further credence to this analysis, we test two other variables that are known to covary along with rain rates: Droplet concentration and CLWP, as independently observed by MODIS and longer-wavelength channels of the AMSR/E instrument, respectively. More intense rain should be associated with more cloud water content and should act to scavenge cloud drops, leading to a reduction in N_d (Wood, 2006). Figure 11 shows the 12-hr ($t = -12$ to $t = 0$) Lagrangian changes seen in rain rate and CLWP anomalies for wind speed anomaly bins at $t = -12$. Figure 11 is produced for overcast closed cell MCC (CC>90%). Also shown is the Lagrangian 24-hr N_d change seen from $t = -24$ to $t = 0$. A 24-hr change is used because there are no N_d estimates for nocturnal data from MODIS. Results show consistency between all three variables, with stronger winds associated with more intense rain, increasing CLWP, and decreasing N_d.

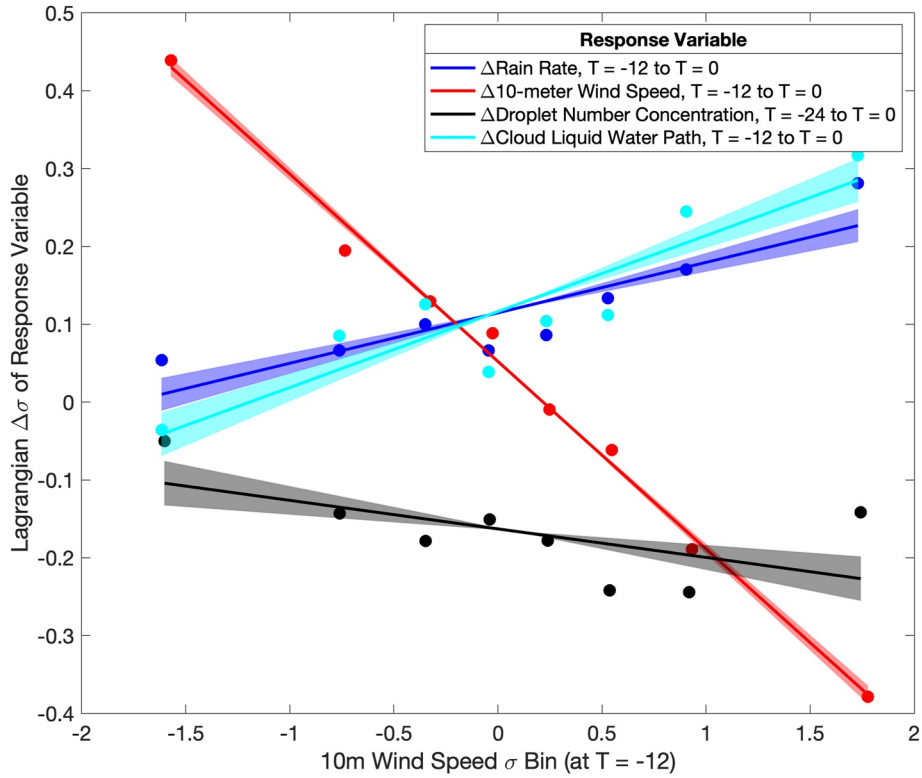

Figure 11. The 12-hr Lagrangian response ($t = -12$ to $t = 0$ *hr*) of wind speed anomalies (red), rain rate anomalies (dark blue), cloud liquid water path anomalies (cyan), and the 24-hr Lagrangian change ($t = -24$ to $t = 0$ *hr*) in N_d (black) for σ bins of wind speed anomaly at time $t = -12$.

In Figure 11 we do not account for red noise behavior as in Figure 7, where a residual Lagrangian change in rain rate is shown. This is done in order to further test data validity: If intense rain and strong wind were conflated due to both being inferred by warm T_b, then not only would their values tend to correlate positively, but their Lagrangian tendencies would also correlate positively, so that an observed decrease in wind would coincide with an observed decrease in rain rate. Figure 11 shows that the opposite occurs. After the observation at $t = -12$ *hr*, wind speed is shown to strongly decline between $t = -12$ and $t = 0$ *hr*. This decline in wind speed is an expected result given the tendencies of cloud and environmental variables to regress to their mean values from initial extremes (Eastman et al., 2016). Rain rate and CLWP increase during this same period, however, showing behavior inconsistent with a bias caused by warm T_b being misattributed to rain rate and wind speed.

The wind and rain relationship could also be biased by other meteorological variables covarying with wind speed. This was tested for by stratifying wind and rain data within bins of potential meteorological confounders that covary with wind speed (as shown in supplementary Figure 2). Bin boundaries are $-2 < \sigma' < -1$, $-1 < \sigma' < 0$, $0 < \sigma' < 1$, and $1 < \sigma' < 2$, where σ' represents the anomaly of each confounding variable. Confounders tested include subsidence at 700 hPa, SST, q_{700}, RH_{1000}, LTS, and divergence of the wind field at 1,000 hPa. The wind and rain relationship remained consistently positive within each bin of each confounder. This test for the effects of confounding variables was not possible for the analyses in Figures 5 and 6 due to small sample sizes when subsetting in bins of confounders. Those results may be somewhat ambiguous, particularly for the several meteorological variables predicting the C-D transition, which tend to covary. All of these variables are associated with a deepening and drying PBL, so an assumption of increased entrainment drying appears reasonable.

An additional source of possible bias in satellite retrieved rain rates, CLWP, and N_d is potential differences in mean cloud amount for differing trajectory sets. The presence of cloud edges in broken scenes can artificially affect these variables, leading to artificial differences seen between trajectory sets. To study whether these biases could be present in this study, Figure 12 compares mean σ values of composited variables (along y) as a function of cloud cover controlled for in bins (along x) for two trajectory sets: one that shows the 24-hr C-O transition, and

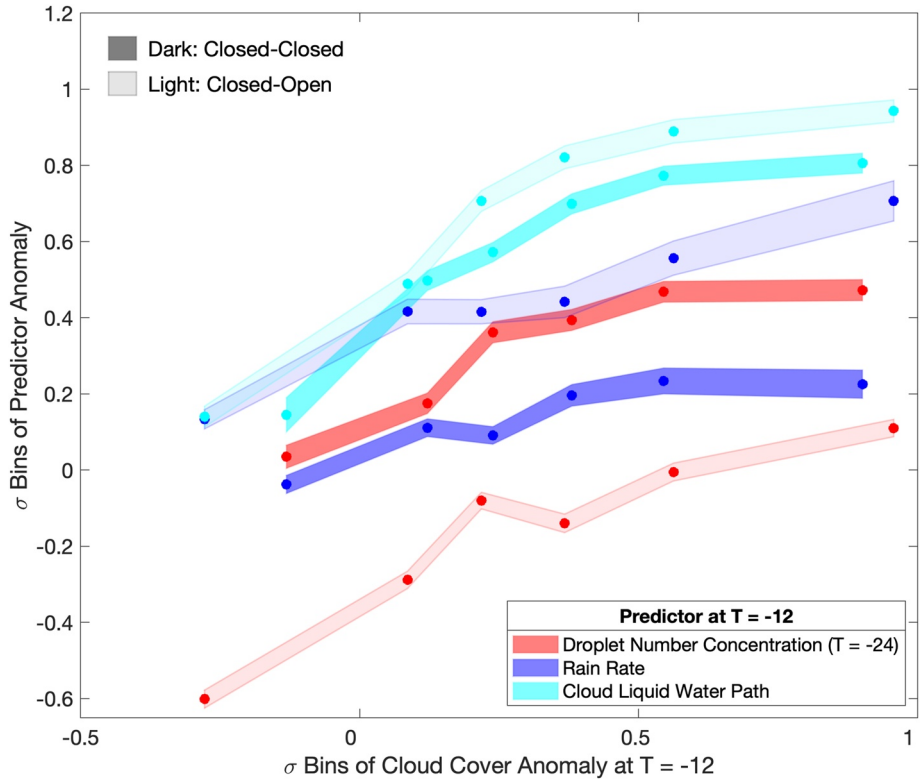

Figure 12. Rain rate (dark blue) at $t = -12$, cloud liquid water path (cyan) at $t = -12$, and Nd (red) at $t = -24$ *hr* for two sets of trajectories that evolve from $t = -24$ to $t = 0$: a C-O (light) set and a C-C (dark) set. Trajectory sets are stratified (along-x) by cloud cover anomaly observed at $t = -12$. Results show that variable values for these trajectory sets are significantly different even when cloud cover is held constant. Plot width represents the standard error of the mean.

another set that remains closed cell MCC, without a transition (C-C). Mean values of N_d, CLWP, and rain rate anomalies (*y* axis) are plotted for each set as a function of cloud cover anomaly (*x* axis). The figure shows that when cloud cover is held constant, differences remain between sets for rain rate and CLWP at $t = -12$ *hr*, and also for N_d at $t = -24$ *hr*. These results show that a cloud-amount bias is not causing differences in our predictor variables that could bias our conclusions. This analysis was repeated while controlling for CLWP along x, and results were qualitatively unchanged, as shown in supplementary Figure 3.

4.2. Rain Rate, LWP, and N_d

Figure 11 shows that strong wind speed is, on average, followed by increases in CLWP and rain rate, along with decreasing N_d, all of which appear to predict the C-O transition. A question motivated by this figure is whether N_d is truly a predictor of the C-O transition, or if it is simply covarying along with rain rate through precipitation scavenging. The power of low N_d to predict the C-O transition appears strong enough (nearly as strong as rain rate) in Figure 5a to motivate additional scrutiny. In Figure 13, the relationship between N_d, CLWP, and rain rate is explored in an instantaneous (non-Lagrangian) framework to contrast rain rates for varying N_d and CLWP conditions. Raw values and original units are used instead of anomalies and σ bins for Figures 13a and 13b in order to produce values more easily compared to other future studies. In Figure 13a rain rate is plotted as a function of variable N_d within σ bins of relatively constant CLWP. In Figure 13b, rain rate is plotted as a function of CLWP within σ bins of relatively constant N_d. Lines are fit to the rain rate/N_d relationships in 13a and the rain rate/CLWP relationships in 13b. In frame 13c, the slopes from 13a and 13b are averaged and compared. Units of N_d and CLWP in 13c are standardized by dividing original units by the variables' standard deviation, so we can compare the instantaneous changes in mean rain rate associated with varying N_d values against rain rate changes for varying CLWP values.

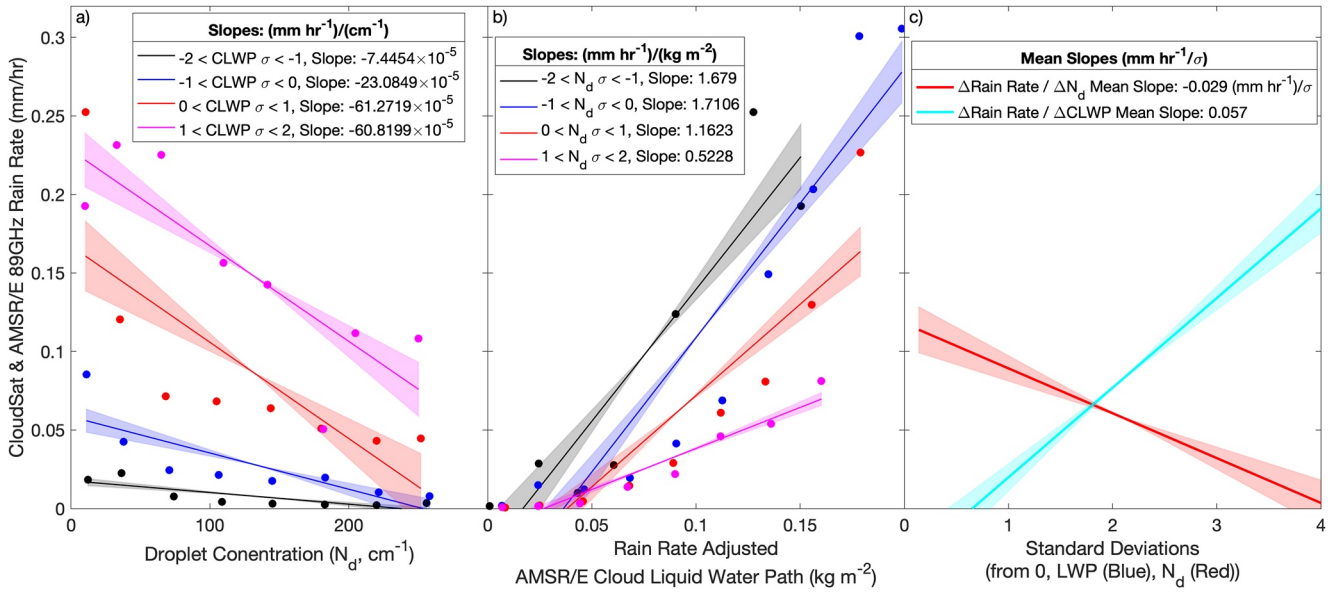

Figure 13. (a) Rain Rate (*y* axis) as a function of N_d (*x* axis) for sigma bins of cloud liquid water path (CLWP) with a linear fit and confidence bounds. (b) Rain rate (*y* axis) as a function of CLWP (*x* axis) for sigma bins of Nd, with linear fit and confidence bounds. (c) The mean slope and confidence bounds from (a, red) and (b, cyan), with values along x standardized in order to compare slopes. Raw values (not anomalies) in a stationary (Eulerian, NOT Lagrangian framework) are shown here in order to produce values more easily comparable to future work. Data are for overcast (CC>90%), closed cell MCC.

Results from Figures 13a and 13b suggest that decreased droplet concentration and increased CLWP are associated with more intense rain. This figure also allows us to see the effects of CLWP and N_d on rain rate when the other variable is controlled in σ bins, with bin boundaries $-2 < \sigma \leq -1$, $-1 < \sigma \leq 0$, $0 < \sigma \leq 1$, and $1 < \sigma \leq 2$. In comparing the relationships between bins, we can see that the Δrain rate/ΔNd relationship is stronger (steeper slope) when CLWP is higher and the Δrain rate/ΔCLWP is also stronger when N_d is lower. This means that when CLWP is high, rain rate is more sensitive to N_d perturbations, and when N_d is low, rain rate is more sensitive to CLWP perturbations. These results point toward a system potentially containing an internal feedback, where a reduction in N_d (driven by intense rain) can lead to a cloud deck that rains even more intensely for a given CLWP, as suggested by Yamaguchi et al. (2017). This reduced N_d, in turn, would lead to stronger rain rates and further reduced N_d, and may provide a reason that low N_d environments tend to favor the C-O transition. This could loosely be described by the relationship Rain Rate $\propto LWP^a/N_d^b$.

The comparison of mean slopes in Figure 13c shows that a 1-σ change in CLWP is associated with roughly twice the increase in rainfall as a 1-σ decline in N_d, suggesting that while both of these variables are significantly associated with rain rate, CLWP has a stronger association on average (nearly 2x). The stronger relationship between rain rate and CLWP compared to rain rate and Nd is further substantiated and explored in more detail in Pawlowska and Brenguier (2003) and van Zanten et al. (2005).

4.3. Variations in Lagrangian Mesoscale Cloud Morphology Transition Characteristics With Planetary Boundary Layer Depth

Prior work in the literature suggests that PBL depth is an important factor in mesoscale cloud morphology transitions (e.g., Wyant et al., 1997). Our own analysis indicates that these transitions have some sensitivity to PBL depth. We saw in Section 3.3 that C-O transitions are heavily dependent on the amount of moisture in the PBL, the concentration of which will inherently vary with PBL depth. Closed to disorganized transitions, in contrast, are more dependent on meteorological conditions. However, the entrainment drying process identified in Section 3.2 for C-D includes PBL depth as a skilled predictor at lead time $t = -12$ *hr* suggesting it has an important role in this transition. Our analysis thus far does not account for the modulating influence of PBL depth on the skill and influence of other predictor variables. This section investigates whether there are profound differences in the mechanisms driving MCC transitions as the initial PBL depth experienced by the clouds is varied. Figures 14 and 15 test this, where we compare composited predictor variables observed at lead time $t = -12$ *hr* for sets of

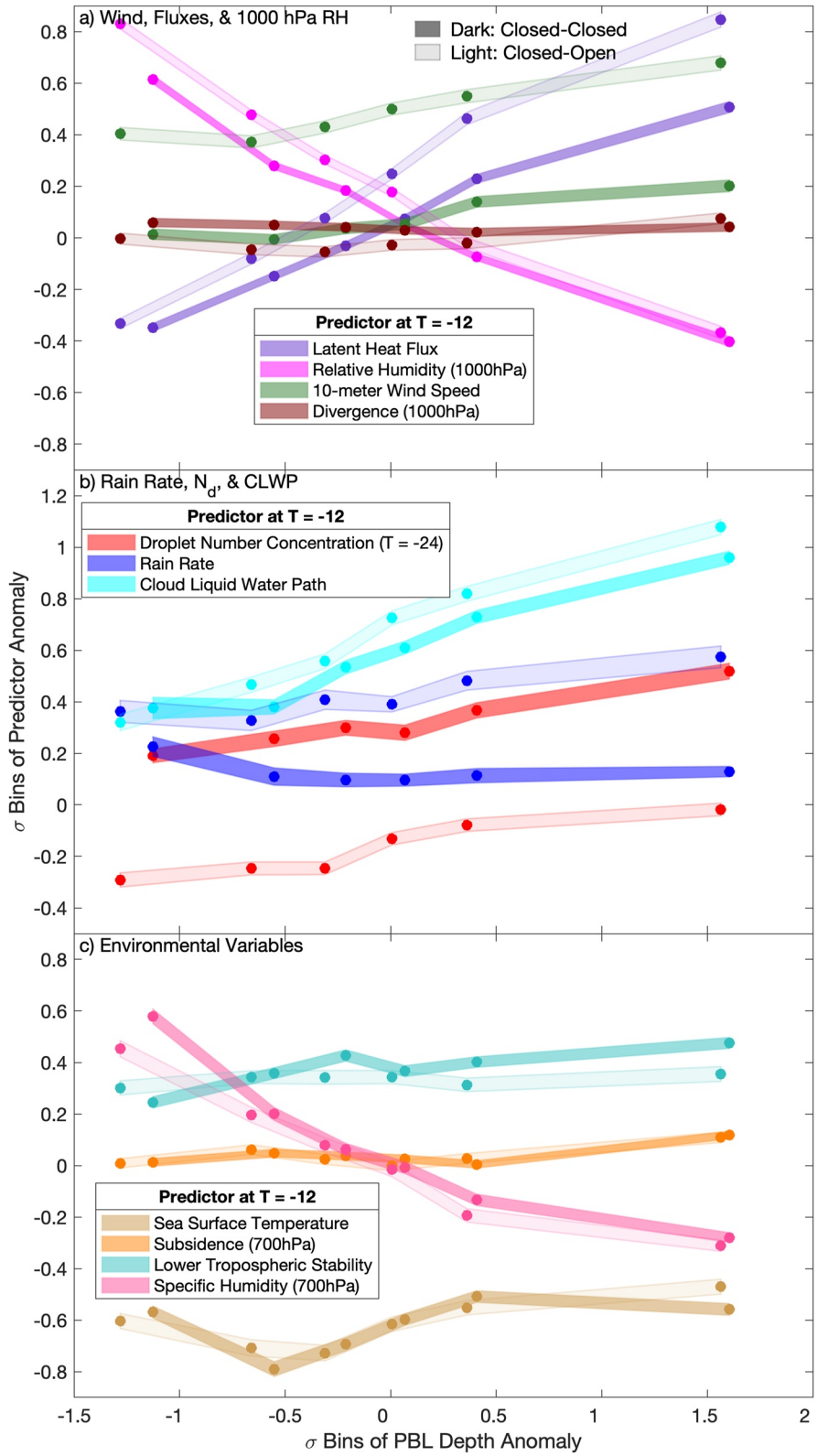

Figure 14. Mean values of anomalies of (a) wind speed, surface wind divergence, latent heat fluxes, and RH_{1000}, (b) rain rate, N_d, and cloud liquid water path, (c) environmental variables: sea surface temperature, 700 hPa subsidence, lower tropospheric stability, and q_{700} at lead time $t = -12$ *hr* for subsets of trajectories that either transition from closed-to-open mesoscale cellular convective (light shading), or remain closed (dark shading) from $t = -24$ to $t = 0$ *hr* for bins of constant planetary boundary layer depth anomaly. Plot width represents the standard error of the mean.

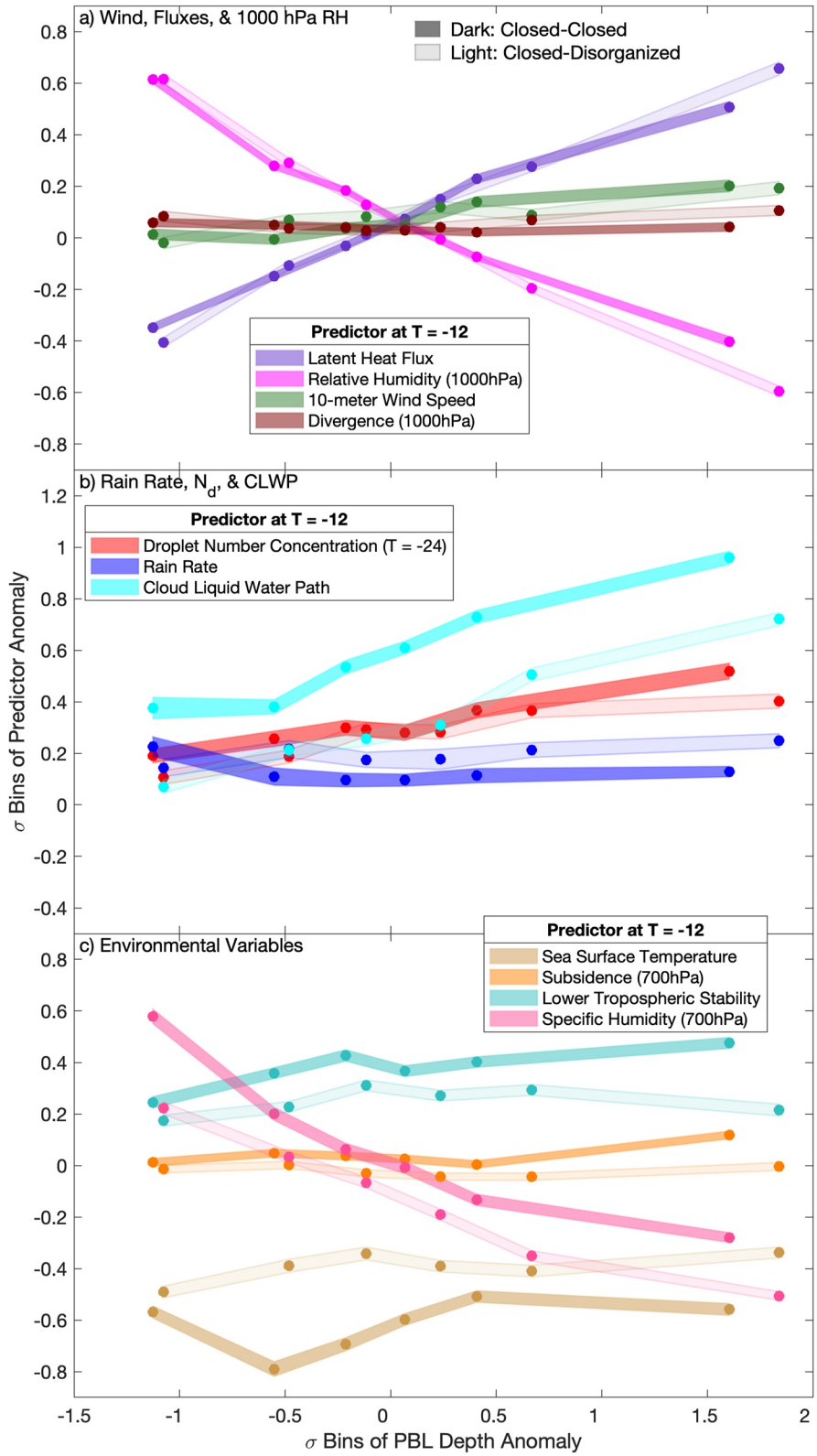

Figure 15. Mean values of anomalies of (a) wind speed, surface wind divergence, latent heat fluxes, and RH_{1000}, (b) rain rate, N_d, and cloud liquid water path, (c) environmental variables: sea surface temperature, 700 hPa subsidence, lower tropospheric stability, and q_{700} at lead time $t = -12$ *hr* for subsets of trajectories that either transition from closed-to-disorganized mesoscale cellular convective (light shading), or remain closed (dark shading) from $t = -24$ to $t = 0$ *hr* for bins of constant planetary boundary layer depth anomaly. Plot width represents the standard error of the mean.

C-O or C-D trajectories versus C-C trajectories for PBL depth bins. Plots represent the mean value of a predictor (*y* axis) for six equally populated bins of varying PBL depths (*x* axis). Six bins were chosen instead of the eight above due to the more limited numbers of observations; limited due to the additional filters necessary to produce PBL depth estimates. Results were qualitatively unaffected by varying bin number, but noise was reduced with fewer bins. The vertical width of the plotted lines represents the standard error of the mean.

Consistent with our earlier analysis demonstrating its predictive skill, Figure 14a shows that wind speed is on average stronger for the C-O trajectory set for all PBL depths compared to the C-C set. Also shown in Figure 14a, RH_{1000} and LHF anomalies vary significantly across bins of constant PBL depths. In shallow PBLs, both C-C and C-O trajectories tend to be more humid, with lower LHF, while the opposite is true in deeper PBLs. This is consistent with a lower-altitude LCL in shallow PBLs, and possibly greater moisture stratification in deeper PBLs. Comparing LHF and RH_{1000} for the two different transition types in 14a, the C-O transition is more strongly associated with higher humidity in shallow PBLs, with smaller differences in LHF. However, in deep PBLs the C-O transition is more strongly associated with greater LHF, while differences in RH are smaller. These relationships remain consistent with the proposed wind speed mechanism for driving anomalous moisture fluxes *or* content, and additionally show that wind may be a stronger signifier of moisture *content* in humid, shallow PBLs, and moisture *flux* in deeper PBLs. The comparison of surface divergence shows that the C-O transition is favored when surface convergence is slightly higher in shallow PBLs.

In Figure 14b, a comparison of N_d, rain rate, and CLWP is made between the C-O and C-C groups for constant PBL depths. Results show that for all PBL depths, the C-O set is consistently rainier, has lower N_d, and has more cloud water compared to the C-C group. Differences in rain rate and CLWP are slightly greater in deeper PBLs. We additionally examine the differences in meteorological variable anomalies across PBL depths: SST, LTS, q_{700}, and 700 hPa subsidence (Figure 14c). Differences between these values for the C-O and C-C sets are nearly negligible. The only small distinctions are in inversion strength and q_{700}, both of which are slightly lower for C-O trajectories compared to C-C. Humidity above the PBL appears to vary the most across the PBL depth spectrum of any of the meteorological variables, with more water vapor overlying anomalously shallow PBLs for both the C-O and C-C sets. This is consistent with prior results in Eastman and Wood (2018) where high overlying humidity was shown to be associated with anomalously shallow PBLs that experienced limited cloud top radiative cooling.

Trajectories showing the C-D transition are compared to non-transitioning C-C trajectories in Figure 15, using the same constant-PBL framework as Figure 14. Significant differences are apparent between Figures 14 and 15. The C-D trajectory sets in Figure 15 tend to be offset to the right relative to the C-C sets, indicating that the distributions of PBL depths for the C-D sets are consistently deeper compared to the C-C sets. In Figure 15a, the C-C and C-D trajectory sets show similar LHF, RH_{1000}, wind speed, and convergence anomalies for bins of constant PBL depth, indicating that these mechanisms have much less effect on the C-D transition, unlike the C-O transition shown in 14a. Differences in rain rate and N_d between C-C and C-D trajectory sets appear minimal in Figure 15b, while CLWP appears significantly lower for the C-D set compared to the C-C set. In Figure 15c, the C-D and C-C trajectory sets show significant separation when comparing anomalies of environmental variables. The C-D trajectory sets are associated with warmer SST, a drier free troposphere, slightly less subsidence, and a weaker inversion compared to the C-C trajectories. Figure 15c shows significant contrast with Figure 14c, where these environmental variables were nearly overlapping for the C-C and C-O sets.

Figures 14 and 15 show strong contrasts between the mechanisms associated with the C-O and C-D transitions. The C-O transition is more strongly associated with increased moisture flux in deep PBLs and increased RH_{1000} in shallow PBLs, with strong winds associated with the increased moisture regardless of PBL depth. This increased moisture in the C-O transition is evident with higher CLWP and stronger rain rates. In contrast to the C-O transition, environmental processes that warm and dry the boundary layer are associated with the C-D transition. This is shown in the reduced CLWP, warmer SST, weaker inversion and subsidence, and drier overlying atmosphere in the C-D set. The C-D sets plotted in Figure 15 are offset to the right indicating that, on average, the C-D trajectories occur in deeper PBLs; however, the plot also shows that processes that act to dry the cloud layer still tend to drive the C-D transition when PBL depth is controlled for.

4.4. Potential Limitations of Reanalysis Data

This work relies on meteorological variables from the ERA5 reanalysis. The reanalysis data set does not represent low cloud morphology as sensed by MODIS. This introduces the potential for biases in the reanalysis data due to possible differences in the interaction between these morphologically distinct cloud types and the surface or overlying troposphere. This study attempts to control for such biases by aligning all of our data sets at the closed cell state at $t = -24\ hr$ where MODIS observes cloud cover at 90% for all three groups studied (C-C, C-O, and C-D). A check against the ERA5 total cloud cover for these three groups shows that the ERA5 cloud cover is less extensive than MODIS by 6%, 7%, and 9% for C-C, C-O, and C-D, respectively, at $t = -24\ hr$ compared to MODIS. Future research is needed to assess potential biases by comparing reanalysis variables against observed variables for each morphological state.

5. Discussion

This work is a continuation of the Lagrangian analysis presented in Eastman et al. (2021). That work compared composite trajectories for our three trajectory groups: C-O, C-C, and C-D. Results there showed that strong wind, intense rain rates, and low N_d precede the C-O transition by 12–24 hr. Conditions that favor entrainment of dry air into the cloud deck such as declining subsidence, a weak inversion, a dry free troposphere, warm SST, and a deepening PBL precede the C-D transition, also by 12–24 hr. Open questions from that work include "Is wind speed a driver of the closed-open transition, does wind speed have a strong effect on microphysics and/or precipitation, are synoptic differences apparent between longer back trajectories, and what drives the higher LWP and reduced Nd that tends to precede closed-open transitions?" Additionally, the predicting power of variables to drive an MCC transition could not be compared in that work using that composite analysis.

The analysis introduced here substantiates the conclusions in Eastman et al. (2021) and improves upon it in several ways: Expanding trajectory length to 96 hr shows that timescales associated with some predictors are longer than others. Strong winds precede the C-O transition by at least 72 hr, while precipitation, N_d, and CLWP anomalies appear to act on timescales closer to a single day. A similar timescale split exists for variables driving the C-D transition, where warm SST precedes the transition for several days, but processes related to entrainment predict the transition only 1 day in advance. This hints at the existence of a regime/process divide in the behavior of the Sc system, where long-term meteorological regimes (warm SST, or anomalously windy environments in our cases here) favor one MCC transition over the other (the C-D vs. C-O, respectively). Within these multi-day regimes, processes that drive cloud transitions through enhanced entrainment drying, or increased rainfall can then act to modify the clouds during a single diurnal cycle. This is loosely consistent with the fast/slow manifold system envisioned by Bretherton et al. (2010), where thermodynamic adjustments internal to the PBL occur within 24 hr. These results also hint that there are synoptic differences between Sc regimes that favor a transition to open cells versus those that breakup into disorganized MCC.

The analysis presented here allows for the comparison of predicting power for variables tested as drivers of the MCC transition. A more intense rain rate is the strongest predictor of the C-O transition, and warm SST is the strongest driver of the C-D transition.

In directly addressing the remaining open questions from Eastman et al. (2021): Wind speed appears to be a driver of the C-O transition through the modification of moisture in the boundary layer, where strong winds are associated with higher humidity, stronger fluxes, and greater rain rates, as shown in Figure 9. More intense rain rates tend to coincide with a reduction in N_d, which can lead to further enhancements in rain rate as shown in Section 4.2. The increased rain, which is the strongest predictor of the C-O transition, is the likely driver of that transition through the previously theorized cold-pool convergence process described in Section 1, and in Feingold et al. (2010). Wang et al. (2010) also highlight the role of PBL moisture content on rainfall and open cell formation. Here, we build on this by implicating wind speed as a possible modifier of moisture in the PBL.

A possible conceptual model emerges from results presented in this work. Marine stratocumulus may be most persistent when moisture input is well balanced by entrainment of dry air. An imbalance in either moisture flux or entrainment may drive morphological changes. An excess of moisture in the overcast Sc-covered PBL, through wind-driven fluxes, can cause an increase in rain rates, a decline in N_d, stronger rain rates yet, and a change from closed cells to open cell Sc. This transition is similar to that described in Feingold et al. (2010), where evaporative cooling beneath raining Sc cells drives downdrafts that reach the surface, spread laterally, and collide,

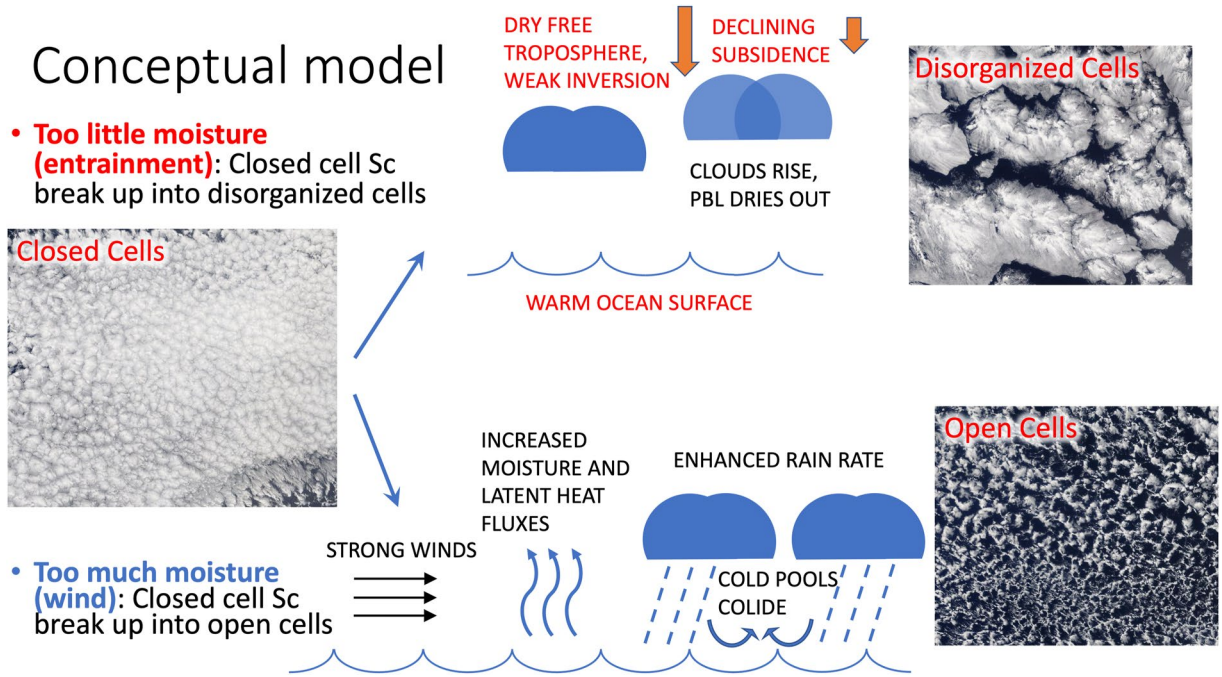

Figure 16. A conceptual model detailing the contrast between mechanisms driving the Lagrangian transitions from closed to open cell mesoscale cellular convective (MCC) compared to closed to disorganized MCC.

causing convergence and rising on the mesoscale. An excess of dry air entrainment may drive the morphological transition from closed cell Sc to disorganized cells. This change appears driven by a drying, warming, and deepening PBL, similar to the transitions described in Wyant et al. (1997), Sandu et al. (2010), and Sandu and Stevens (2011). Those idealized Sc-Cu transitions were forced by a warm sea surface driving increasingly strong updrafts into a decoupling Sc layer, causing increased mixing across the trade inversion, working in concert with weakening subsidence to deepen and decouple the PBL. Here, warm SST is shown to be a robust predictor of this transition, and this work goes on to show that the transition is especially likely in the presence of variables that favor PBL deepening and drying of the cloud through entrainment, such as a weak inversion, dry free troposphere, and weaker subsidence. These mechanisms are simplified and summarized in Figure 16.

Concerning the effects of rainfall on the C-D transition, anomalously intense rainfall significantly predicts the C-O transition, but rainfall does not appear to drive the C-D transition. This suggests that although rain could act as a moisture sink, drying the PBL, this effect is not nearly as strong as entrainment processes at cloud top in predicting the C-D transition.

The role of reduced N_d in favoring the C-O transition may be due to the enhancement of rain rates associated with lower N_d for a constant CLWP, as shown in Figure 13. This is broadly consistent with prior work by Rosenfeld et al. (2012), Wood et al. (2009), and Teller and Levin (2006), who all show that reductions in cloud drop concentrations are associated with more intense rainfall. Rosenfeld et al. (2012) go on to suggest that the C-O transition may be inhibited by increased N_d due to suppressed rain rates while Goren et al. (2019) show that the decline in Sc seen in the daytime portion of the diurnal cycle of Sc occurs later when N_d is higher. Results here appear to substantiate this claim, with the C-O transition favored not only by intense rain rates, but low N_d.

As mentioned in Section 1, several prior publications have noted that stronger winds appear associated with more intense rainfall in both shallow and deep cloud systems (Back & Bretherton, 2005; Lamer et al., 2020; Nuijens et al., 2009; Schulz et al., 2021). Wood et al. (2008) also connects weak wind speeds with environments with less cloud water, higher N_d, and fewer C-O transitions, all results compatible with less rainfall. Jensen et al. (2021) show that windier and rainier environments are associated with the presence of open cell MCC. Our results substantiate these results and propose a mechanism for these relationships: that wind-driven increases in moisture flux and moisture content enhance cloud water and rain rates in an overcast Sc PBL, favoring a C-O transition through the cold-pool convergence mechanism. Currently employed reanalysis data are likely too coarse

to capture this convergence, motivating future studies that can capture the wind fields of transition Sc at higher spatial resolution.

It is likely that other processes can enhance rainfall independently of wind, and could therefore predict the C-O transition, since wind is not driving this transition directly, but is instead part of a two-part process where strong wind enhances rain rates. However, of all variables tested, wind speed distinguished itself as a stronger predictor of the C-O transition than all other variables but rain rate and N_d, which act on shorter timescales. Other meteorological processes, such as surface wind convergence, are likely associated with stronger rainfall, but relationships may not be consistent enough within and between our study regions to show a strong predicting signal of the C-O transition.

The association between rainfall and the C-O transition is shown to exist here and in prior work, but the actual breakup process has not been observed by this analysis in real time. This is due to limitations in using polar orbiting satellites, which only sense the same area twice daily, so all we can conclude is that our results *are consistent with* a cold pool convergence hypothesis. These satellites and their sensors represent the best currently available platform for such an extensive study, given their ability to nearly simultaneously assess cloud liquid water, droplet concentration, rain rates, morphology, and cloud amount. To continue this work, geostationary satellites, with vastly improved temporal resolution, could be employed to precisely pinpoint morphology transitions, as shown by Smalley et al. (2022) in tracking closed-to-open MCC transitions. Coinciding surface observations could then be used to detect evidence of rainfall and cold pool convergence, thereby validating the process proposed here. Additionally, this work can be applied to assess climate model performance. Climate models cannot represent specific morphologies, but tests could assess whether transitions away from overcast Sc are associated with both high flux environments or enhanced entrainment variables and a warm sea surface.

6. Conclusions

The closed to open MCC cloud transition (C-O) is preceded by strong winds and high latent heat flux for lead times of ∼3 days. For lead times of ∼24 hr, it is also associated with higher cloud water content, more intense rain, and lower droplet number concentrations. This is consistent with the precipitation-driven cold-pool collision model of the C-O transition presented by Feingold et al. (2010). The closed to disorganized MCC cloud transition (C-D) is preceded by warm sea surface temperature and a weaker inversion at lead times of ∼2–3 days, by reduced subsidence and a dryer free troposphere at ∼24 hr, and a deep boundary layer and low cloud liquid water path at ∼12 hr. This is consistent with a warming, deepening, and drying process in the PBL, like that presented in Wyant et al. (1997) for the equivalent stratocumulus to cumulus transition examined in the eastern subtropical basins. Both C-O and C-D transitions show variables acting on multiple timescales: meteorological variables indicative of weather "regimes" are associated with breakups at longer timescales while fast-acting, thermodynamic and microphysical cloud processes are associated with cloud breakup on timescales of 12–24 hr.

The primary mechanism identified in the C-O transition is a two-step process where strong winds pump additional moisture into the PBL through latent heating and higher relative humidity at 1,000 hPa. This increase in moisture flux and content not only corresponds to stronger rain rates, but to subsequent *increases* in rain rate as we follow cloud scenes. Increased rain has been seen to coincide with stronger winds in a variety of studies. As described above, increased rainfall likely leads to cold pool convergence and initiates the formation of open cell MCC clouds. This study lacks the temporal and spatial resolution to isolate this exact process but future work with increased resolution, possibly using observations from geostationary satellites, passive microwave data, and surface observations may help confirm this mechanism. Additional scrutiny of potential biases in reanalysis data associated with unrepresented cloud morphologies will also aid future studies.

The C-O transition is shown to occur in shallow and deep PBLs, with RH_{1000} as the primary moisture variable associated with the transition in shallow PBLs, while LHF is the primary moisture variable associated with intense rainfall and the C-O transition in deep PBLs. Stronger winds and more intense rain consistently preceded the C-O transition regardless of PBL depth.

The C-O transition is additionally contrasted against the C-D transition in this study. Breakup in the C-O transition is associated with excess moisture fluxed into the PBL by strong winds, while breakup in the C-D transition is associated with variables that can increase entrainment-driven drying in the PBL. Thus, we find that the mesoscale morphology of subtropical Sc appears to be dependent on the moisture balance in the PBL, which is

sustained by competition between surface winds and entrainment. Sc may be broken up by both too much moisture (e.g., into open MCC clouds) or too little (e.g., into disorganized MCC clouds), two transition outcomes that may both differ in their sensitivity to the changing climate and have profoundly different impacts on the climate system.

Data Availability Statement

ERA Interim data used here are available at: https://www.ecmwf.int/en/forecasts/datasets/reanalysis-datasets/era-interim (Dee et al., 2011). ERA5 data (DOI: 10.5065/D6X34W69) used are available at https://confluence.ecmwf.int/display/CKB/ERA5%3A+data+documentation (Copernicus Climate Change Services, 2017). MODIS collection 6 L3 data are available at: https://ladsweb.modaps.eosdis.nasa.gov/archive/allData/61/MYD08_D3/ (King et al., 2003). MODIS collection 6 L2 data are available at: https://ladsweb.modaps.eosdis.nasa.gov/archive/allData/61/MYD06_L2/ (Platnick et al., 2015). AMSR/E L3 gridded day and night averages from Wentz et al. (2014) are available at: www.remss.com/missions/amsr. AMSR/E 89 GHz Brightness temperatures from Ashcroft and Wentz (2019) are available at: https://nsidc.org/data/AE_L2A/versions/4. CloudSat Rain-Profile (Lebsock & L'Ecuyer, 2011) Data are made available here: https://www.cloudsat.cira.colostate.edu/data-products/2c-rain-profile. CALIPSO Vertical Feature Mask data from Vaughan et al. (2004) are available: https://eosweb.larc.nasa.gov/project/calipso/lidar_l2_vfm_table. The observed PBL height data are processed using the above data sets and is available from the author upon request. Rain rate data are made available through the CloudSat DPC: https://www.cloudsat.cira.colostate.edu/community-products/warm-rain-rate-estimates-from-amsr-89ghz-and-cloudsat MATLAB R2020a was used for programming for this work, under academic license 1094417 at the University of Washington.

Acknowledgments
RE is supported by NASA Grant 80NSSC19K1274. Research by ILM is supported by the NOAA Climate and Global Change Postdoctoral Fellowship Program, administered by UCAR's Cooperative Programs for the Advancement of Earth System Science (CPAESS) under award no. #NA18NWS4620043B. Additionally, we thank Stephen Warren, Lynn McMurdie, Dennis Hartman, and Georgy Manucharyan for additional insights and editing on this project.

References

Ashcroft, P., & Wentz, F. J., (2019). AMSR-E/Aqua L2A Global swath spatially-resampled brightness temperatures, Version 4. [Dataset]. NASA National Snow and Ice Data Center Distributed Active Archive Center. https://doi.org/10.5067/YL62FUZLAJUT

Back, L. E., & Bretherton, C. S. (2005). The relationship between wind speed and precipitation in the Pacific ITCZ. *Journal of Climate*, *18*(20), 4317–4328. https://doi.org/10.1175/JCLI3519.1

Bennartz, R. (2007). Global assessment of marine boundary layer cloud droplet number concentration from satellites. *Journal of Geophysical Research*, *112*(D2), D02201. https://doi.org/10.1029/2006JD007547

Boers, R., Acarreta, J. A., & Gras, J. L. (2006). Satellite monitoring of the first indirect aerosol effect: Retrieval of the droplet concentration of water clouds. *Journal of Geophysical Research*, *111*(D22), D22208. https://doi.org/10.1029/2005JD006838

Bretherton, C. S., McCoy, I. L., Mohrmann, J., Wood, R., Ghate, V., Gettelman, A., et al. (2019). Cloud, aerosol, and boundary layer structure across the northeast Pacific stratocumulus to cumulus transition as observed during CSET. *Monthly Weather Review*, *147*(6), 2083–2103. https://doi.org/10.1175/mwr-d-18-0281.1

Bretherton, C. S., Uchida, J., & Blossey, P. (2010). Slow manifolds and multiple equilibria in stratocumulus-capped boundary layers. *Journal of Advances in Modeling Earth Systems*, *2*(14). https://doi.org/10.3894/JAMES.2010.2.14

Copernicus Climate Change Service (C3S). (2017). ERA5: Fifth generation of ECMWF atmospheric reanalyses of the global climate. Copernicus Climate Change Service Climate Data Store (CDS) [Dataset]. https://doi.org/10.5065/D6X34W69

Dee, D. P., Uppala, S. M., Simmons, A. J., Berrisford, P., Poli, P., Kobayashi, S., et al., (2011). The ERA-Interim reanalysis: Configuration and performance of the data assimilation system [Dataset]. Quarterly Journal of the Royal Meteorological Society, *137*(656), 553–597. https://doi.org/10.1002/qj.828

Eastman, R., Lebsock, M., & Wood, R. (2019). Warm rain rates from AMSR-E 89-GHz brightness temperatures trained using CloudSat rain-rate observations. *Journal of Atmospheric and Oceanic Technology*, *36*(6), 1033–1051. https://doi.org/10.1175/JTECH-D-18-0185.1

Eastman, R., & Wood, R., (2016). Factors controlling low-cloud evolution over the eastern subtropical oceans: A Lagrangian perspective using the A-Train Satellites. *Journal of Atmospheric Science*, *73*, 331–351. https://doi.org/10.1175/JAS-D-15-0193.1

Eastman, R., & Wood, R. (2018). The competing effects of stability and humidity on subtropical stratocumulus entrainment and cloud evolution from a Lagrangian perspective. *Journal of the Atmospheric Sciences*, *75*(8), 2563–2578. https://doi.org/10.1175/JAS-D-18-0030.1

Eastman, R., Wood, R., & Bretherton, C. S. (2016). Time scales of clouds and cloud-controlling variables in subtropical stratocumulus from a Lagrangian perspective. *Journal of the Atmospheric Sciences*, *73*(8), 3079–3091. https://doi.org/10.1175/JAS-D-16-0050.1

Eastman, R. I., McCoy, L., & Wood, R. (2021). Environmental and internal controls on Lagrangian transitions from closed cell mesoscale cellular convection over subtropical oceans. *Journal of the Atmospheric Sciences*, *78*, 2367–2383. https://doi.org/10.1175/JAS-D-20-0277.1

Feingold, G., Koren, I., Wang, H., Xue, H., & Brewer, W. A. (2010). Precipitation-generated oscillations in open cellular cloud fields. *Nature*, *466*(7308), 849–852. https://doi.org/10.1038/nature09314

Goren, T., Kazil, J., Hoffmann, F., Yamaguchi, T., & Feingold, G. (2019). Anthropogenic air pollution delays marine stratocumulus break-up to open-cells. *Geophysical Research Letters*, *46*(23), 14135–14144. https://doi.org/10.1029/2019GL085412

Hartmann, D. L., & Short, D. A. (1980). On the use of Earth radiation budget statistics for studies of clouds and climate. *Journal of the Atmospheric Sciences*, *37*(6), 1233–1250. https://doi.org/10.1175/1520-0469(1980)037<1233:otuoer>2.0.co;2

Hubanks, P. A., King, M. D., Platnick, S., & Pincus, R. (2008). MODIS atmosphere L3 gridded product. *NASA Algorithm Theoretical Basis Doc. ATBD-MOD-30*, *90*.

Jensen, M. P., Ghate, V. P., Wang, D., Apoznanski, D. K., Bartholomew, M. J., Giangrande, S. E., et al. (2021). Contrasting characteristics of open- and closed-cellular stratocumulus cloud in the eastern North Atlantic. *Atmospheric Chemistry and Physics*, *21*(19), 14557–14571. https://doi.org/10.5194/acp-21-14557-2021

King, M. D., Menzel, W. P., Kaufman, Y. J., Tanré, D., Gao, B. C., Platnick, S., et al. (2003). Cloud and aerosol properties, precipitable water, and profiles of temperature and humidity [Dataset]. IEEE Transactions on Geoscience and Remote Sensing, *41*(2), 442–458. https://doi.org/10.5067/MODIS/MYD08_D3.006

Krueger, A. F., & Fritz, S. (1961). Cellular cloud patterns revealed by Tiros I. *Tellus*, *13*(1), 1–7. https://doi.org/10.3402/tellusa.v13i1.9440

L'Ecuyer, T. S., Hang, Y., Matus, A. V., & Wang, Z. (2019). Reassessing the effect of cloud type on Earth's energy balance in the age of active spaceborne observations. Part I: Top of atmosphere and surface. *Journal of Climate*, *32*(19), 6197–6217. https://doi.org/10.1175/JCLI-D-18-0753.1

Lamer, K., Naud, C. M., & Booth, J. F. (2020). Relationships between precipitation properties and large-scale conditions during subsidence at the eastern North Atlantic observatory. *Journal of Geophysical Research: Atmospheres*, *125*(7). https://doi.org/10.1029/2019jd031848

Lebsock, M. D., & L'Ecuyer, T. S. (2011). The retrieval of warm rain from CloudSat [Dataset]. Journal of Geophysical Research, *116*(D20), D20209, https://doi.org/10.1029/2011JD016076

McCoy, I. L., Wood, R., & Fletcher, J. K. (2017). Identifying meteorological controls on open and closed mesoscale cellular convection associated with marine cold air outbreaks. *Journal of Geophysical Research: Atmospheres*, *122*(21), 11678–11702. https://doi.org/10.1002/2017JD027031

Mohrmann, J., Wood, R., Yuan, T., Song, H., Eastman, R., & Oreopoulos, L. (2021). Identifying meteorological influences on marine low-cloud mesoscale morphology using satellite classifications. *Atmospheric Chemistry and Physics*, *21*(12), 9629–9642. https://doi.org/10.5194/acp-21-9629-2021

Norris, J. (1998). Low cloud type over the ocean from surface observations. Part II: Geographical and seasonal variations. *Journal of Climate*, *11*(3), 383–403. https://doi.org/10.1175/1520-0442(1998)011<0383:LCTOTO>2.0.CO;2

Nuijens, L., Stevens, B., & Siebesma, A. P. (2009). The environment of precipitating shallow cumulus convection. *Journal of the Atmospheric Sciences*, *66*(7), 1962–1979. https://doi.org/10.1175/2008JAS2841.1

O, K.-T., Wood, R., & Bretherton, C. S. (2018). Ultraclean layers and optically thin clouds in the stratocumulus-to-cumulus transition. Part II: Depletion of cloud droplets and cloud condensation nuclei through collision–coalescence. *Journal of the Atmospheric Sciences*, *75*(5), 1653–1673. https://doi.org/10.1175/JAS-D-17-0218.1

O, K.-T., Wood, R., & Tseng, H. (2018). Deeper, precipitating PBLs associated with optically thin veil clouds in the Sc-Cu transition. *Geophysical Research Letters*, *45*(10), 5177–5184. https://doi.org/10.1029/2018gl077084

Oreopoulos, L. (2005). The impact of subsampling on MODIS level-3 statistics of cloud optical thickness and effective radius. *IEEE Transactions on Geoscience and Remote Sensing*, *43*(2), 366–373. https://doi.org/10.1109/TGRS.2004.841247

Pawlowska, H., & Brenguier, J.-L. (2003). An observational study of drizzle formation in stratocumulus clouds for general circulation model (GCM) parameterizations. *Journal of Geophysical Research*, *108*(D15), 8630. https://doi.org/10.1029/2002JD002679

Platnick, S., Ackerman, S. A., King, M. D., Meyer, K., Menzel, W. P., Holz, R. E., et al. (2015). MODIS atmosphere L2 cloud product (06_L2). NASA MODIS adaptive processing system [Dataset]. Goddard Space Flight Center, USA. https://doi.org/10.5067/MODIS/MOD06_L2.006

Possner, A., Eastman, R., Bender, F., & Glassmeier, F. (2020). Deconvolution of boundary layer depth and aerosol constraints on cloud water path in subtropical stratocumulus decks. *Atmospheric Chemistry and Physics*, *20*(6), 3609–3621. https://doi.org/10.5194/acp-20-3609-2020

Rosenfeld, D., Wang, C. H., & Rasch, P. J. (2012). The roles of cloud drop effective radius and LWP in determining rain properties in marine stratocumulus. *Geophysical Research Letters*, *39*(13), L13801. https://doi.org/10.1029/2012GL052028

Sandu, I., & Stevens, B. (2011). On the factors modulating the stratocumulus to cumulus transitions. *Journal of the Atmospheric Sciences*, *68*(9), 1865–1881. https://doi.org/10.1175/2011JAS3614.1

Sandu, I., Stevens, B., & Pincus, R. (2010). On the transitions in marine boundary layer cloudiness. *Atmospheric Chemistry and Physics*, *15*(5), 2377–2391. https://doi.org/10.5194/acp-10-2377-2010

Schulz, H., Eastman, R., & Stevens, B. (2021). Characterization and evolution of organized shallow convection in the downstream north Atlantic trades. *Journal of Geophysical Research: Atmospheres*, *126*(17), e2021JD034575. https://doi.org/10.1029/2021JD034575

Scott, R. C., Myers, T. A., Norris, J. R., Zelinka, M. D., Klein, S. A., Sun, M., & Doelling, D. R. (2020). Observed sensitivity of low cloud radiative effects to meteorological perturbations over the global oceans. *Journal of Climate*, *33*(18), 7717–7734. https://doi.org/10.1175/JCLI-D-19-1028.1

Smalley, K. M., Lebsock, M. D., Eastman, R., Smalley, M., & Witte, M. K. (2022). A Lagrangian analysis of pockets of open cells over the south-eastern Pacific. *Atmospheric Chemistry and Physics*, *22*(12), 8197–8219. https://doi.org/10.5194/acp-22-8197-2022

Teller, A., & Levin, Z. (2006). The effects of aerosols on precipitation and dimensions of subtropical clouds: A sensitivity study using a numerical cloud model. *Atmospheric Chemistry and Physics*, *6*, 67–80. https://doi.org/10.5194/acp-6-67-2006

Terai, C. R., & Wood, R. (2013). Aircraft observations of cold pools under marine stratocumulus. *Atmospheric Chemistry and Physics*, *13*(19), 9899–9914. https://doi.org/10.5194/acp-13-9899-2013

van Zanten, M. C., Stevens, B., Vali, G., & Lenschow, D. H. (2005). Observations of drizzle in nocturnal marine stratocumulus. *Journal of the Atmospheric Sciences*, *62*(1), 88–106. https://doi.org/10.1175/JAS-3355.1

Vaughan, M., Young, S., Winker, D., Powell, K., Omar, A., Liu, Z., et al. (2004). Fully automated analysis of space-based Lidar data: An overview of the CALIPSO retrieval algorithms and data products [Dataset]. SPIEThe, *5575*, 16–30. Retrieved from https://eosweb.larc.nasa.gov/project/calipso/lidar_l2_vfm_table

Wang, H., Feingold, G., Wood, R., & Kazil, J. (2010). Modelling microphysical and meteorological controls on precipitation and cloud cellular structures in Southeast Pacific stratocumulus. *Atmospheric Chemistry and Physics*, *10*(13), 6347–6362. https://doi.org/10.5194/acp-10-6347-2010

Warren, S. G., Eastman, R., & Hahn, C. J. (2007). A survey of changes in cloud cover and cloud types over land from surface observations, 1971–1996. *Journal of Climate*, *20*(4), 717–738. https://doi.org/10.1175/JCLI4031.1

Wentz, F. J., & Meissner, T. (2004). AMSR-E/Aqua L2B Global swath ocean products derived from Wentz algorithm. Version 2. L3 LWP [Dataset]. https://doi.org/10.5067/AMSR-E/AE_OCEAN.002

Wentz, F. J., Meissner, T., Gentemann, C., & Brewer, M. (2014). Remote Sensing Systems AQUA AMSR-E [Daily] Environmental Suite on 0.25 deg grid [Dataset]. Remote Sensing Systems. http://www.remss.com/missions/amsr

Wood, R. (2006). Rate of loss of cloud droplets by coalescence in warm clouds. *Journal of Geophysical Research*, *111*(D21), D21205. https://doi.org/10.1029/2006JD007553

Wood, R. (2012). Stratocumulus clouds. *Monthly Weather Review*, *140*(8), 2373–2423. https://doi.org/10.1175/MWR-D-11-00121.1

Wood, R., Comstock, K. K., Bretherton, C. S., Cornish, C., Tomlinson, J., Collins, D. R., & Fairall, C. (2008). Open cellular structure in marine stratocumulus sheets. *Journal of Geophysical Research*, *113*(D12), D12207. https://doi.org/10.1029/2007JD009371

Wood, R., & Hartmann, D. L. (2006). Spatial variability of liquid water path in marine low cloud: The importance of mesoscale cellular convection. *Journal of Climate*, *19*(9), 1748–1764. https://doi.org/10.1175/JCLI3702.1

Wood, R., O, K. T., Bretherton, C. S., Mohrmann, J., Albrecht, B. A., Zuidema, P., et al. (2018). Ultraclean layers and optically thin clouds in the stratocumulus-to-cumulus transition. Part I: Observations. *Journal of the Atmospheric Sciences*, *75*(5), 1631–1652. https://doi.org/10.1175/jas-d-17-0213.1

Wood, R. T., Kubar, L., & Hartmann, D. L. (2009). Understanding the importance of microphysics for warm rain in marine low clouds. Part II: Heuristic models of rain formation. *Journal of the Atmospheric Sciences*, *66*(10), 2973–2990. https://doi.org/10.1175/2009JAS3072.1

Wyant, M. C., Bretherton, C. S., Rand, H. A., & Stevens, D. E. (1997). Numerical simulations and a conceptual model of the stratocumulus to trade cumulus transition. *Journal of the Atmospheric Sciences*, *54*(1), 168–192. https://doi.org/10.1175/1520-0469(1997)054<0168:NSAACM>2.0.CO;2

Yamaguchi, T., & Feingold, G. (2015). On the relationship between open cellular convective cloud patterns and the spatial distribution of precipitation. *Atmospheric Chemistry and Physics*, *15*(3), 1237–1251. https://doi.org/10.5194/acp-15-1237-2015

Yamaguchi, T., Feingold, G., & Kazil, J. (2017). Stratocumulus to cumulus transition by drizzle. *Journal of Advances in Modeling Earth Systems*, *9*(6), 2333–2349. https://doi.org/10.1002/2017MS001104

Zhou, X., & Bretherton, C. S. (2019). Simulation of mesoscale cellular convection in marine stratocumulus: 2. Nondrizzling conditions. *Journal of Advances in Modeling Earth Systems*, *11*(1), 3–18. https://doi.org/10.1029/2018MS001448